

# Nanostructured CMOS Wireless Ultra-Wideband Label-Free PCR-Free DNA Analysis SoC

Hamed Mazhab Jafari, *Student Member, IEEE*, Karim Abdelhalim, *Student Member, IEEE*, Leyla Soleymani, Edward H. Sargent, Shana O. Kelley, and Roman Genov, *Senior Member, IEEE*

**Abstract**—A fully integrated 54-channel wireless fast-scan cyclic voltammetry DNA analysis SoC is presented. The microsystem includes 546 3D nanostructured and 54 2D gold DNA sensing microelectrodes as well as 54 pH sensors. Each channel consists of a chopper-stabilized current conveyer with dynamic element matching. It is utilized as the amperometric readout circuit with a linear resolution from 8.6 pA to 350 nA. The on-chip programmable waveform generator provides a wide range of user-controlled rate and amplitude parameters with a maximum scan range of 1.2 V, and scan rate ranging between 0.1 mV/sec to 300 V/sec. A digital ultra-wideband transmitter based on a delay line architecture provides wireless data communication with data rates of up to 50 Mb/sec while consuming 400  $\mu$ W. The 3 mm  $\times$  3 mm prototype fabricated in a 0.13  $\mu$ m standard CMOS technology has been validated in prostate cancer synthetic DNA detection with 10 nM label-free PCR-free detection limit. Each channel occupies an area of only 0.06 mm<sup>2</sup> and consumes 42  $\mu$ W of power from a 1.2 V supply.

**Index Terms**—Biosensor, cyclic voltammetry, DNA, electrochemical sensor, nano-structured electrodes, ultra-wideband transmitter.

## I. INTRODUCTION

**A**NALYSIS of specific biomolecules, such as proteins and nucleic acids, finds applications that range from disease diagnostics to forensics. Detection, identification, and quantification of nucleic acid sequences such as DNA, messenger RNA (mRNA), and micro-RNA have recently been exploited for the diagnosis, prognosis, and treatment choices for heredity and infectious diseases [1], [2], the monitoring of the quality of food and water [3], and the detection of bio-warfare agents [6].

DNA is a nucleic acid that contains the genetic blueprint required for development and functioning of the living organisms. DNA is composed of two polymer strands made of units called

Manuscript received November 13, 2012; revised July 04, 2013; accepted March 04, 2014. Date of publication April 11, 2014; date of current version April 21, 2014. This paper was approved by Associate Editor Ken Shepard. This work was supported by Natural Sciences and Engineering Research Council of Canada (NSERC).

H. M. Jafari, K. Abdelhalim, T. Sargent, and R. Genov are with the Department of Electrical and Computer Engineering, University of Toronto, Toronto, ON M5S 3G4, Canada (email: hamed@eecg.utoronto.ca).

L. Soleymani is with the Department of Engineering Physics, McMaster University, Hamilton, ON L8S 4L7, Canada.

S. O. Kelley is with the Faculty of Pharmacy, University of Toronto, Toronto, ON M5S 3G4, Canada

Color versions of one or more of the figures in this paper are available online at <http://ieeexplore.ieee.org>.

Digital Object Identifier 10.1109/JSSC.2014.2312571

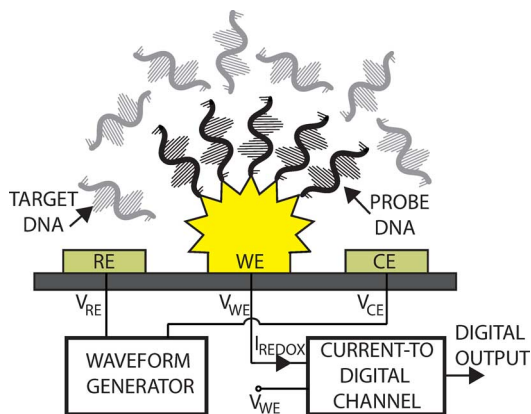


Fig. 1. Conceptual view of an amperometric DNA sensing microsystem.

nucleotides. The backbone of DNA is made of sugars and phosphate groups joined by ester bonds. Each nucleotide consists of three units: a phosphate group, a 2-deoxyribose group, and a nitrogen base group. The phosphate group loses a proton in a neutral solution giving rise to the overall negative charge of the DNA. The nucleotide units in DNA include adenine (A), cytosine (C), guanine (G), and thymine (T). The four bases are bonded to the sugar/phosphate DNA backbone to form the complete nucleotide [7]. DNA does not exist as a single molecule in any living organism, but exists as a pair of molecules that are bonded together. Two long strands of DNA are twisted together like vines, in the shape of a double helix. The double-stranded DNA (DSDNA) is stabilized by hydrogen bonds between nucleotides [8]. The DSDNA molecule can be separated into two single-stranded DNA (SSDNA) molecules in a process called de-naturing. De-naturing is normally achieved by heating the DSDNA. In reverse, two complementary SSDNA molecules can form a DSDNA molecule in a process known as hybridization or renaturation [8].

If nucleic acid detection is to be widely used globally and at the point of care, the detection process has to offer high throughput and automated, portable analysis at a low cost. A number of lab-on-a-chip systems have been developed that translate nucleic hybridization events to electrical [5], optical [4], magnetic [9], and gravimetric [14] signals. These systems typically feature an array of single-stranded nucleic acid probe DNA sequences that are immobilized on a solid surface. At the time of the capture of complementary target sequences through Watson Crick base pairing, the sensor transduces a measurable signal. Watson Crick base pairing involves hydrogen

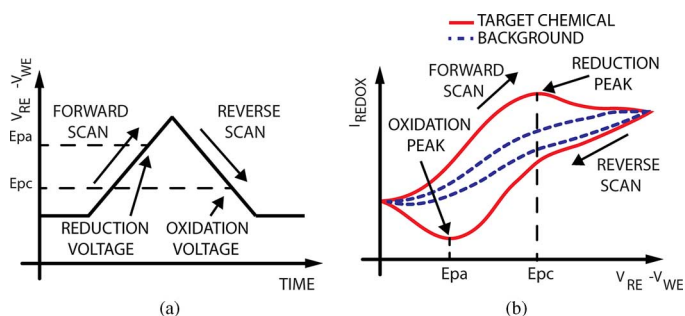


Fig. 2. Fast-scan cyclic voltammetry principle of operation (a) Cyclic redox potential applied between the reference and working electrode. (b) Cyclic voltammogram in the absence (background) and presence of the target chemical.

bonding between complementary SSDNA base pairs resulting in double-stranded DNA which includes the target DNA strand bonded to the probe DNA strand on the same solid surface.

The polymerase chain reaction (PCR) is commonly utilized to increase the concentration of the target DNA in a sample, thus increasing the detection accuracy. PCR is a procedure in biochemistry to amplify a single or a few copies of a DNA sequence, generating up to millions of copies of the same DNA sequence [10], [11]. This method relies on thermal cycling which consists of cycles of repeated heating and cooling for DNA melting and enzymatic replication of the DNA. This is generally costly and time consuming.

Signal transduction is often performed by coupling the target sequence with a reduction-oxidation (redox) or fluorescent label with a well-defined and easily detected electrochemical or optical signature, respectively. This is known as label-based sensing which requires sample labeling and the corresponding cost and time.

Label-free detection of DNA hybridization is also possible, by monitoring the electrical signals, such as current, voltage, impedance, and conductance, at the sensor's solid-liquid interface. There are several label-free electrical nucleic acid detection platforms [12], [13], but these techniques rely on off-chip, expensive, and bulky instrumentation for signal readout and processing, characteristics that make the techniques unsuitable for many point-of-need and in-field applications.

Amperometric electrochemical DNA sensors [15], [19]–[22], [30], [32]–[34] have emerged as a low-cost, high-throughput, and real-time alternative to conventional optical and electrochemical sensory methods. Electrochemical amperometric DNA analysis techniques have the potential to provide real-time, label-free, PCR-free sensing in portable detection platforms.

A block diagram of a three-electrode electrochemical amperometric sensing system is depicted in Fig. 1. It consists of a working electrode (WE), a reference electrode (RE), a counter electrode (CE), a waveform generator and a current-to-digital channel. In this configuration the working electrode is held at a known potential,  $V_{WE}$ , by the channel and the redox current generated due to the voltage difference between the working and reference electrodes is recorded. The counter electrode provides the current required to keep the voltage difference be-

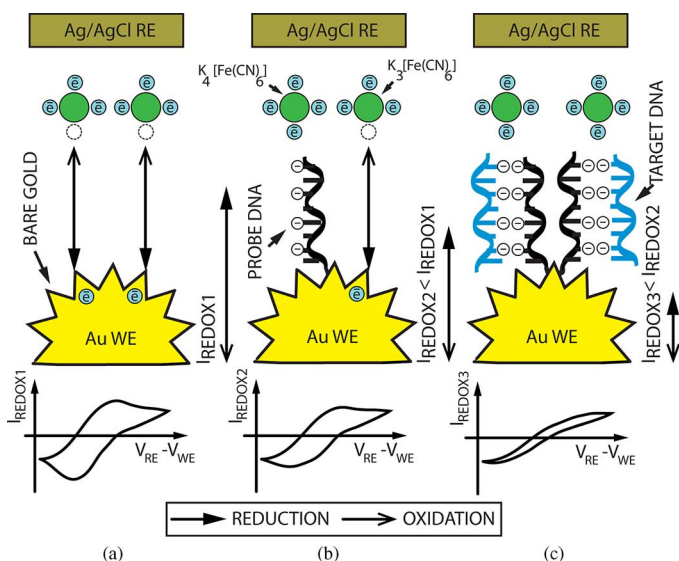


Fig. 3. Label-free electrochemical DNA detection principle. (a) Bare electrode: maximum charge transfer between working and reference electrode in the absence of negatively charged probe and target DNA; (b) non-complementary target DNA: reduction in the charge transfer rate due to the presence of negatively charged probe DNA, and (c) complementary DNA: further reduction in the charge transfer rate due to the presence of negatively charged target and probe DNA.

tween the working and reference electrodes accurate. In electrochemical DNA sensing applications the working electrode is coated with a probe DNA. Binding of the probe DNA with the target DNA results in variation of the working electrode surface properties such as impedance or surface charge. The variation of the surface properties results in a change in the recorded value and waveform features of the redox current, thus indicating the thermodynamics and kinetics of chemical reactions at the sensory interface. In most biochemical sensing applications the recorded redox current is in the range of 100 pA to 100 nA [24], [26], [27]. The reference electrode is set to a constant voltage for constant-potential amperometry (CA) [25], a sinwave for impedance spectroscopy (IS) [42], or a bidirectional ramp voltage for fast-scan cyclic voltammetry (CV) [25] which offers higher chemical selectivity.

In the CV method, a cyclic ramp potential is intermittently applied between the working and reference electrodes, as shown for one period in Fig. 2(a). The time between two such scans, which can vary, determines the temporal resolution of the technique. The halt time prevents successive scans from influencing each other. The cyclic voltammogram shown in Fig. 2(b), represents the redox current versus the applied redox potential and provides unique information about the chemical substance under measurement. For example, the location of the reduction and oxidation peaks acts as a chemical identifier for various chemicals. The reduction and oxidation peak amplitudes are different for different chemical concentrations. A parasitic background current is also generated due to the transient changes of the applied voltage (Fig. 2(b)). This current occurs mainly because of the charging and discharging of the double layer capacitance associated with the electrode-electrolyte interface, not due to sensing. The background current

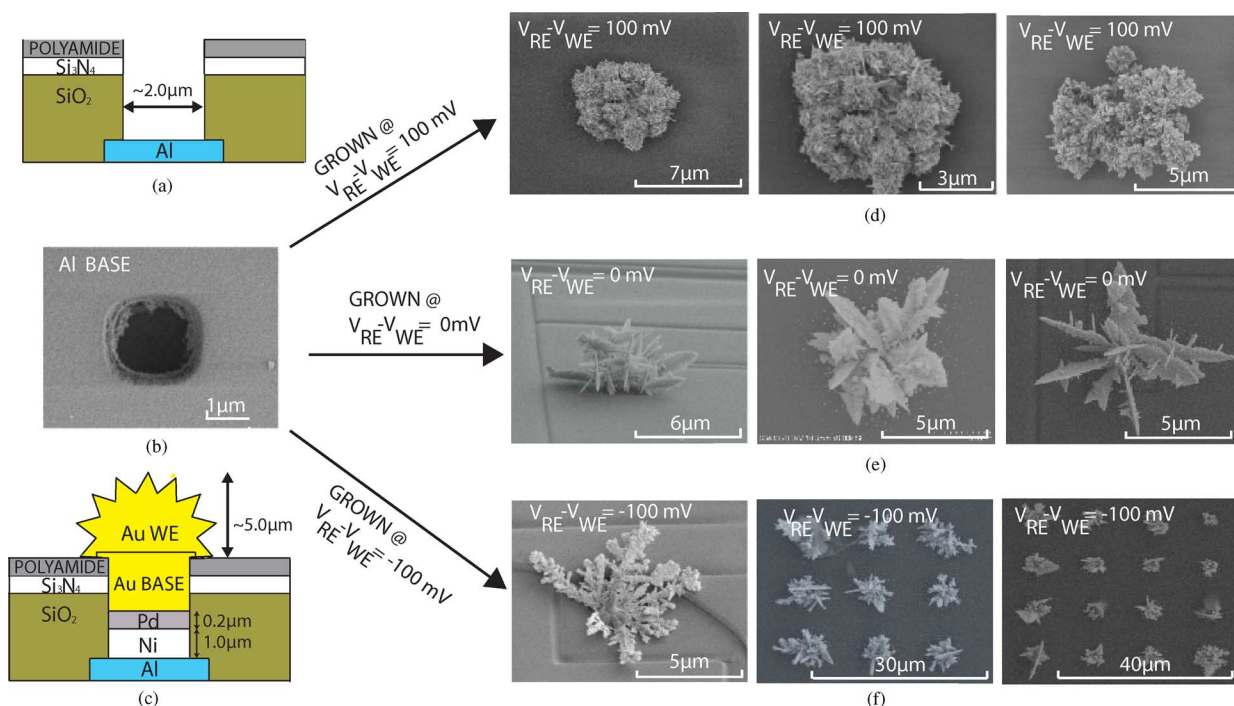


Fig. 4. Nanostructured DNA sensing working electrodes (NMEs): (a) Cross-sectional view of a  $2 \mu\text{m} \times 2 \mu\text{m}$  passivation opening in standard CMOS, (b) SEM photograph of a  $2 \mu\text{m} \times 2 \mu\text{m}$  working electrode passivation opening over an aluminum base, (c) nanostructured  $2 \mu\text{m} \times 2 \mu\text{m}$  working electrode grown on the passivation opening over an aluminum base in standard CMOS, (d) and (e) SEM photographs of nanostructured microelectrodes grown at different electrodeposition conditions on the passivation opening in (b).

is proportional to the scan rate, and also to the double layer capacitance and has to be subtracted out.

Several electrochemical DNA detection CMOS microsystems have been recently reported [30]–[35]. The design in [30] is a 50-channel programmable electrochemical biosensor array implemented in a  $0.13 \mu\text{m}$  standard CMOS technology. The microsystem includes flat gold electrodes and analog recording channels, and utilizes impedance spectroscopy for DNA detection. The implementation in [31] consists of one recording channel and  $24 \times 16$  recording electrodes implemented in a  $0.5 \mu\text{m}$  CMOS technology. The design, which consists of a three-electrode regulation loop and an analog recording channel, utilizes CV for DNA detection and analysis. A 128-channel DNA analysis microsystem implemented in a  $0.5 \mu\text{m}$  CMOS technology in [32] consists of on-chip gold electrodes, a three-electrode regulation loop, and an in-pixel ADC. The design presented in [33] is implemented in a  $0.5 \mu\text{m}$  CMOS technology and consists of 24 recording channels with an in-channel ADC,  $24 \times 24$  polymer-functionalized sensing electrodes, and a temperature sensor. The microsystem utilizes CV for DNA detection and analysis. The design in [34] presents the first fully-integrated CMOS DNA analysis microsystem, which consists of 16 recording channels, a three-electrode regulation loop, a flat gold DNA sensing microelectrode, and an in-channel ADC. A 40-channel DNA system-on-chip (SoC) based on ion-sensitive field-effect transistor (ISFET) sensors for rapid point-of-care DNA detection is reported in [35]. The design includes an in-channel delta-sigma ADC, temperature sensors, and heaters. Among these the lowest DNA concentration detectable on CMOS is  $10 \text{ nM}$ .

The wireless communication capability is necessary in applications such as at-home health monitoring, food safety control and water quality monitoring where in-field DNA sensing and analysis on a disposable platform are required. Recently, a wireless single-channel DNA detection system-on-chip has been reported [36]. The design utilizes polysilicon nanowires as DNA sensors and includes an on-chip temperature sensor and a wireless OOK transmitter.

We have reported in Nature Nanotechnology amperometric electrochemical sensors fabricated on passive silicon, not on CMOS, that do not require cumbersome tagging of DNA with chemical or optical labels [37]. These gold microelectrodes have fine-tuned nanostructured patterns on their surface that yield an over 140 dB input dynamic range and  $10 \text{ aM}$  detection limit sufficient for PCR-free DNA detection.

In this paper, we present a  $0.13 \mu\text{m}$  CMOS DNA analysis SoC with 600 such nanostructured microelectrodes (NMA) grown directly on the die. This paper extends on an earlier report of the principle and demonstration in [38], and offers a more detailed analysis of the design and additional experimental results characterizing the circuit implementation and the DNA detection performance. This SoC performs label-free PCR-free DNA analysis using fast-scan cyclic voltammetry with a  $10 \text{ aM}$  detection limit and pH sensing for cancer detection. The microsystem consists of a fully programmable arbitrary waveform generator with an on-chip memory and 54 chopper-stabilized current recording channels. The chopper-stabilized current conveyer front-end, with an input-referred noise of  $0.13 \text{ pA}_{\text{rms}}$  over one kHz bandwidth, is utilized as the amperometric readout circuit in each channel. The current conveyer achieves

linear resolution from 10 pA to 400 nA. A chopper-stabilized dual-slope ADC is utilized to digitize the recorded current. The waveform generator provides stimulation waveforms with a maximum scan range of 1.1 V and a scan rate ranging from 0.1 mV/sec to 300 V/sec. A fully digital 10 Mb/s ultra-wideband (UWB) transmitter performs wireless communication.

The rest of this paper is organized as follows. Section II provides background on DNA detection principles. Section III describes the process of fabrication of the nanostructured DNA sensing microelectrodes. Section IV presents the DNA analysis SoC VLSI architecture. Section V details the circuit implementation of the VLSI architecture. Section VI demonstrates the electrical experimental results obtained from the 0.13  $\mu\text{m}$  CMOS prototype. In Section VII, the results of on-chip electrochemical recording of calibration chemicals are presented. In Section VIII, the results of on-chip CV recording of a synthetic DNA marker in prostate cancer screening are presented.

## II. DNA DETECTION PRINCIPLE

The principle of the label-free DNA detection method based on potassium ferricyanide reporter is shown in Fig. 3. Potassium ferricyanide  $\text{K}_4[\text{Fe}(\text{CN})_6]$  is a negatively charged redox complex with a well-defined electrochemical signature exhibiting oxidation and reduction currents at  $V_{RE}-V_{WE}$  voltage of  $-450$  mV and  $-250$  mV, respectively. Maximum electron transfer between the bare gold electrode and potassium ferricyanide is achieved in the absence of both the DNA target and probe, as denoted by  $I_{REDOX1}$ , in Fig. 3(a). Electron transfer is decreased when a negatively charged self-assembled monolayer of probe DNA (SSDNA) is deposited on the electrode, as shown in Fig. 3(b). This corresponds to smaller redox current  $I_{REDOX2}$ , which results in relatively smaller reduction or oxidization peaks. Upon bonding of the probe DNA and target DNA (if present) the resulting DSDNA is more negatively charged and causes potassium ferricyanide to be repelled farther from the electrode surface reducing the generated faradaic current, as shown in Fig. 3(c). The redox current  $I_{REDOX3}$  is significantly smaller compared to the first two cases and lacks the reduction and oxidation peaks. In other words, the presence of negatively charged DNA on the biosensor surface translates to a decrease in the potassium ferricyanide oxidation/reduction current creating a detectable signal change [39]–[41].

## III. INTEGRATED SENSORS

### A. DNA Sensing Microelectrodes

To improve the sensitivity and dynamic range of the DNA sensor, nanostructured microelectrodes (NMEs) [37] are grown on the CMOS aluminum working electrode base, using a combination of electroless plating and electroplating techniques.

It is shown in [37] that nanostructuring the working electrode allows for fabrication of DNA sensors on passive silicon that have a broad range of sensitivities and dynamic ranges. Highly branched electrodes with fine nanostructuring are capable of

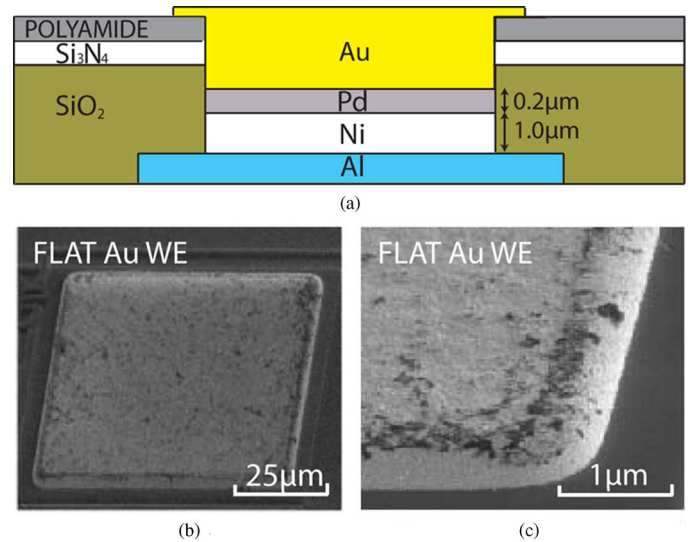


Fig. 5. (a) Passivation opening in standard CMOS and added metal layers of a flat (2D) microelectrode after electroless nickel-palladium-gold plating, (b) and (c) SEM photographs of such  $55 \mu\text{m} \times 55 \mu\text{m}$  working electrodes.

achieving a 10 aM detection limit [37]. It is postulated that the DNA probes which are functionalized on nanostructured electrodes are more accessible and, as a result, bond much easier and faster with target molecules. Microelectrodes with different degrees of nanostructuring result in different sensitivities and dynamic ranges. By placing an array of different electrodes on the same CMOS chip the sensor system can achieve a sensitivity of two to six orders of magnitude [37].

In this design DNA sensing working electrodes are created by forming  $2 \mu\text{m} \times 2 \mu\text{m}$  passivation openings on the top metal layer (aluminum) of the CMOS chip (as it is commonly done for bond pads) as shown in Fig. 5(a) and (b). An electroless metal plating technique is employed to sequentially deposit nickel (Ni), palladium (Pd) and then flat gold (Au) base on the exposed Al surface to form an electrode foundation as shown in Fig. 4(c). Next NMEs are grown electrostatically in a solution containing 69  $\mu\text{L}$  of gold solution (544385–10 G Aldrich) diluted in 2.5 mL of deionized (DI) water 2.5 mL of 5  $\mu\text{M}$  HCl [37] as also shown in Fig. 4(c). The shape and the size (defining the sensitivity and dynamic range) of the NMEs depend on the potential difference between the working electrode and the reference electrode and the duration of the electroplating. Examples of NMEs grown on a CMOS chip for 60 sec at 100 mV, 0 and  $-100$  mV voltage difference between an on-chip Au working electrode and an off-chip (Ag/AgCl) reference electrode are shown in Fig. 4(d)–(f), respectively. Two examples of arrays of NMEs grown on a CMOS chip are also shown in Fig. 4(f), middle and right. For comparison purposes, large flat (2D) working electrodes have also been fabricated on-CMOS. These flat gold electrodes are fabricated using the same electroless plating technique as that used for the NME foundation fabrication, as shown in Fig. 5(a). For example, the SEM photographs of such a gold-plated  $55 \mu\text{m} \times 55 \mu\text{m}$  on-CMOS flat working electrode are shown in Fig. 5(b) and (c).

## B. PH Sensors

The in-channel ion-sensitive-field-effect-transistor (ISFET) based pH sensor is implemented by a floating gate PMOS with the size of  $0.5 \mu\text{M} \times 0.35 \mu\text{M}$ . The poly-gate of the PMOS is connected to the top metal layer to form a floating gate electrode, and the CMOS passivation layer ( $\text{Si}_3\text{N}_4$  and  $\text{SiO}_2$ ) is used as the pH-sensitive membrane [53]. It is shown in [52] that the passivation layer (exposed section where there is no polyamide) gives a linear pH response with a sensitivity of approximately  $56 \text{ mV/pH}$  [53], depending on the stoichiometry of the passivation layer. The 54 pH sensors are directly interfaced to the 54 current-recording channels. The source of the PMOS is connected to the VDD (1.2 V), and the drain is connected to the input of a current conveyer. The pH sensor gate voltage is set by the on-chip reference electrode. In this configuration, both the  $V_{gs}$  and the  $V_{ds}$  of the pH sensor PMOS transistor are fixed. Any change in the pH level effectively changes the PMOS threshold voltage. This change results in a corresponding change in the drain current, which is digitized by the recording channel.

## IV. VLSI ARCHITECTURE

### A. Top-Level VLSI Architecture

The top-level VLSI architecture of the wireless DNA analysis SoC is shown in Fig. 6. The SoC consists of 54 current-to-digital recording channels. Each channel is multiplexed between a bank of DNA sensors and a pH sensor.

The sensors are interrogated by the on-chip arbitrary waveform generator that is shared among all channels. The arbitrary waveform generator consists of a 8-bit R-2R DAC, an 8-bit up-down counter and a 3-electrode-configuration RE voltage regulation circuit [42]. The waveform generator provides stimulation waveforms with a maximum scan range of 1.1 V and the scan rate ranging from 0.1 mV/sec to 300 V/sec. It consumes  $900 \mu\text{A}$  from a 1.2 V supply when driving a 5 nF load at the maximum scan rate of 300 V/sec. This maximum rate is not required for the DNA sensing application as the scan rate is limited to low 100 s of mV/sec. Other amperometric biochemical sensing applications (such as, for example, neurotransmitter sensing [25]) require much higher scan rates of up to 300 V/sec. The microsystem presented here is designed so that it can also be used in applications other than DNA sensing. As a result, the waveform generator is designed such that it meets requirements for a general purpose biochemical sensing microsystem but with the power scaling with the frequency. The digital data representing the stimulation waveform properties are stored in the on-chip waveform generator SRAM (Fig. 6).

A current conveyer is placed at the front-end of each channel to acquire the resulting sensory current at a low impedance. A dual-slope ADC quantizes the input redox current and outputs a corresponding digital word. The digital output of each channel is serialized on the chip and is wirelessly transmitted at a data rate of up to 10 Mbps, using an all-digital ultra-wide band transmitter. To enable independent channel programmability, each channel also includes a bias voltage generation cir-

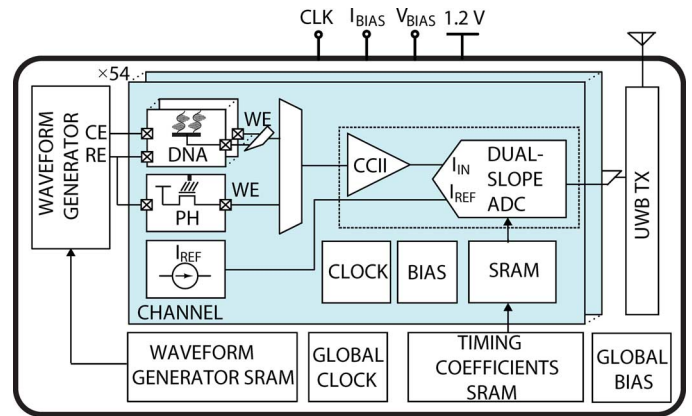


Fig. 6. Wireless DNA analysis microsystem functional block diagram.

cuit, a clock generation circuit, and an in-channel SRAM for setting the channel dynamic range and sensitivity.

### B. Channel VLSI Architecture

The top-level VLSI architecture of one current-to-digital channel of the integrated electrochemical sensory microsystem is shown in Fig. 7. Each channel consists of a chopper-stabilized bidirectional current conveyer (Fig. 7, left) and a 9-bit dual-slope ADC (Fig. 7, right).

The current conveyer buffers the input current and maintains the working electrode at a fixed potential,  $V_{WE}$ , as needed to induce a redox reaction. DNA analysis applications require both sourcing and sinking the redox current. A number of current conveyer designs for electrochemical sensing applications have been reported [43]–[46]. In general, existing designs do not support bidirectional current recording and suffer from the amplifier flicker noise and the mismatch within current mirrors. Fig. 7 (left) depicts a low-noise and accurate current conveyer VLSI architecture that overcomes these limitations. Internal OTA chopper stabilization is utilized to reduce the effect of flicker noise. The current conveyer utilizes low-current regulated-cascode current mirrors to record small (i.e., as small as 10 pA) bidirectional currents. Dynamic element matching is utilized to improve the accuracy by averaging the mismatch in the current mirrors.

The current conveyer is comprised of a PMOS and an NMOS transistors  $M_n$  and  $M_p$  connected in the feedback of the chopper-stabilized OTA. The negative feedback ensures a known potential,  $V_{WE}$ , at the working electrode is set by the voltage at the negative terminal of the OTA. It also enables the current conveyer to source and sink input current without the need for a DC offset current [43], which can disturb the DNA charge balance. The currents through  $M_n$  and  $M_p$  are mirrored by dynamically-matched current mirrors to the output of the current conveyer and are added.

Based on previously published results of DNA hybridization experiments on NME working electrodes [37], it is determined that the on-chip ADCs must be able to digitize bidirectional current in the 10 pA to 100 nA range or greater, and to cover a frequency range of 0.01 Hz to at least 1 kHz. The dual-slope ADC architecture is selected for this purpose because its dy-

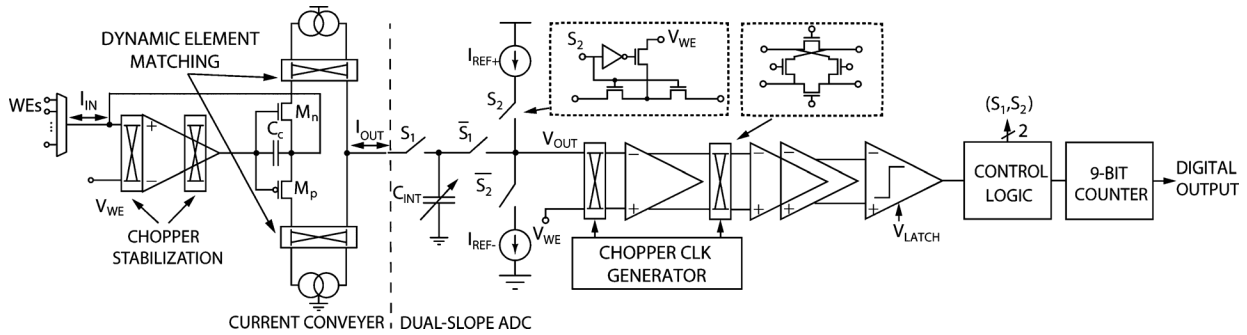


Fig. 7. Simplified top-level VLSI architecture of one chopper-stabilized integrated current-to-digital channel.

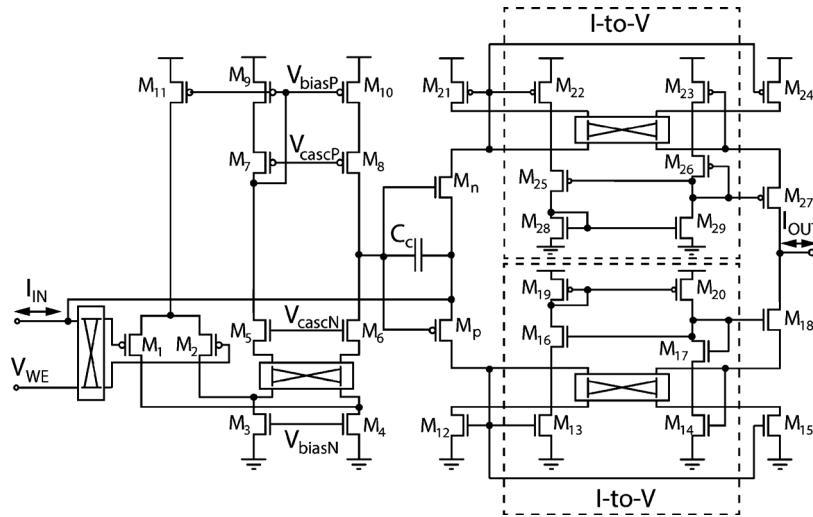


Fig. 8. Detailed implementation of the current conveyor OTA with internal chopping and dynamically-matched low-current regulation.

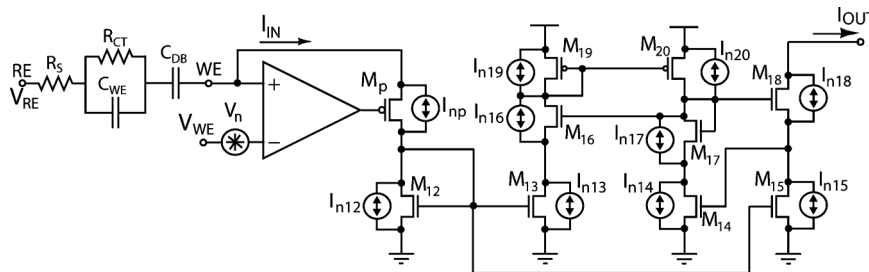


Fig. 9. Simplified noise model of the chopper-stabilized current conveyor.

dynamic range, sampling frequency, and nominal resolution suit these requirements and can all be easily adjusted.

The dual-slope ADC shown in Fig. 7 (right) consists of an integrating on-chip variable capacitor  $C_{INT}$  (adjustable from 1 pF to 10 pF, all the measurements here are done using a 2 pF capacitor value), regulated-cascode current sources  $I_{REF+}$  and  $I_{REF-}$ , a four-stage track-and-latch comparator, a 9-bit digital counter and control logic. All switches are implemented as low-leakage switches as shown in an inset in Fig. 7. The reference current sources are implemented as regulated-cascode current mirrors to ensure accurate current sourcing over the operating dynamic range. The  $I_{REF+}$  is implemented with PMOS devices and the  $I_{REF-}$  is implemented with NMOS devices. This can result in some mismatch between the  $I_{REF+}$  and  $I_{REF-}$ . The

effect of the mismatch between the positive and negative current source does affect the linearity of the ADC. These effects are within the specification and are reflected in the measured spectrum of the ADC output and its ENOB presented in Section VI. The first stage of the comparator is chopper-stabilized to reduce the effect of its offset and low-frequency noise.

The dual-slope ADC operates in two phases. In phase one, the integrating capacitor  $C_{INT}$  is charged by the input current  $I_{IN}$  for a predetermined period of time  $T_1$ . Next, during the second phase of the operation, the capacitor is discharged to zero by a DC reference current  $I_{REF}$  ( $I_{REF+}$  or  $I_{REF-}$ ). By counting the duration of the second phase, the time  $T_2$ , a digital representation of  $I_{IN}$  can thus be obtained as  $-\text{sign}(I_{REF}) \times (T_2/T_1) \times |I_{REF}|$ . In this design the value of the  $I_{REF}$  is

programmable (using an off-chip variable resistor) between 100 pA to 50 nA.

The in-channel SRAM can also be used to adjust the duration of the charging and discharging cycles of the dual-slope ADC for the purpose of channel gain calibration. For example if  $I_{REF}$  is higher in the first channel compared to the second channel, then the duration of the charging time  $T_2$  can be reduced for the first channel to compensate for larger  $I_{REF}$  and thus generating the same output digital code for both channels for a given input current. This effectively calibrates each channel independently and reduces the channel-to-channel gain mismatch.

## V. CIRCUIT IMPLEMENTATION

### A. Current Conveyor

As shown in Fig. 8 the OTA has been implemented as a folded-cascode amplifier to provide a wide input dynamic range and a high gain. In this design, internal OTA chopping has been implemented to reduce the effect of both flicker noise and the input offset voltage. A set of chopper switches are placed at the input of the OTA. Another set is placed after the NMOS tail current source. This significantly reduces the flicker noise and offsets due to the input pair transistors and the NMOS tail current source transistors. Minimum size switches are utilized to reduce the effect of charge injection into the working electrode. The output current mirrors are implemented using a low-current regulated cascode topology. The regulated current mirrors  $M_{12}$ ,  $M_{15}$ ,  $M_{18}$  and  $M_{21}$ ,  $M_{24}$ ,  $M_{27}$  replicate  $I_{IN}$  (fed through the NMOS and PMOS transistors) at the output node with a high output impedance. The I-to-V blocks consisting of transistors  $M_{13,14,16,17,19,20}$  and  $M_{22,23,25,26,28,29}$  adjust the gate voltage of the NMOS and PMOS output cascode transistors  $M_{18}$  and  $M_{27}$  such that the drain-source voltages of the current mirror transistor pairs  $M_{12}$ ,  $M_{15}$  and  $M_{21}$ ,  $M_{24}$  are pairwise equal thus ensuring accurate current copying down to the pA level.

Mismatch in these regulated cascode current sources can significantly reduce the linearity of the current conveyor. Dynamic element matching (DEM) [48] is employed to reduce the effect of the mismatch in the current mirrors. The main source of mismatch in the regulated cascode current mirrors is due to the mismatch in the transistor pairs  $M_{12}$ ,  $M_{15}$  and  $M_{21}$ ,  $M_{24}$ . To reduce the effect of the mismatch between these transistors, the DEM technique is applied by means of the chopper switches at the drains of the current source transistors, so that the critical transistor pairs are dynamically matched. In this method, the locations of the transistors  $M_{12}$ ,  $M_{15}$  and  $M_{21}$ ,  $M_{24}$  are swapped periodically, at 500 Hz, effectively averaging the current mirrors mismatch. Ideally the error due to the mismatch in the current mirrors is reduced with a higher DEM switching frequency which results in better averaging over one ADC conversion cycle. Due to the non-ideality of the switches, an increase in the switching frequency results in high-frequency switching noise and an increase in the charge injected into the current path. This in turn causes an error at the output of the current conveyor. Based on these considerations the 500 Hz DEM frequency was chosen.

To achieve efficient flicker noise reduction, the chopper frequency needs to be higher (at least twice) than the input signal

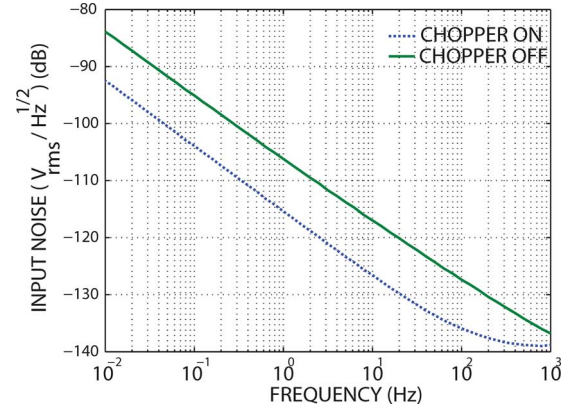


Fig. 10. Simulated input-referred noise spectrum of the current conveyor from 0.01 Hz to 1 kHz.

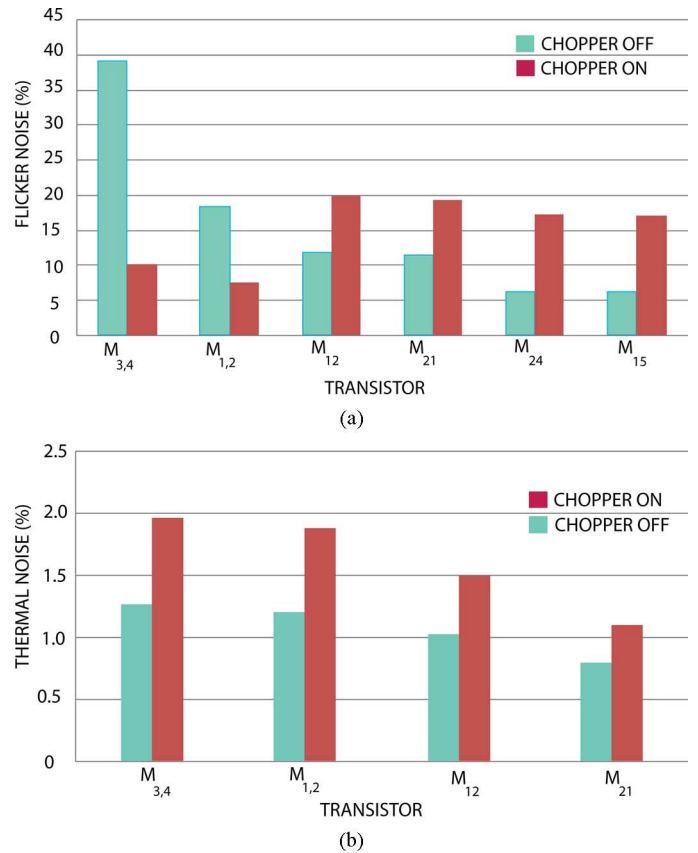


Fig. 11. Current conveyor noise summary: (a) flicker noise contributions, and (b) thermal noise contributions.

maximum frequency (1 kHz). The chopper clock frequency was set to 10 kHz to place the switching noise well outside the operating frequency range. As a result the current conveyor bandwidth should be higher compared to the case where no chopper stabilization is utilized so that the output settles in each switching period. The current conveyor 3 dB bandwidth is 35.7 kHz.

### B. Channel Noise Analysis

An important consideration in the design of the current conveyor is its intrinsic noise as it limits the sensitivity of the

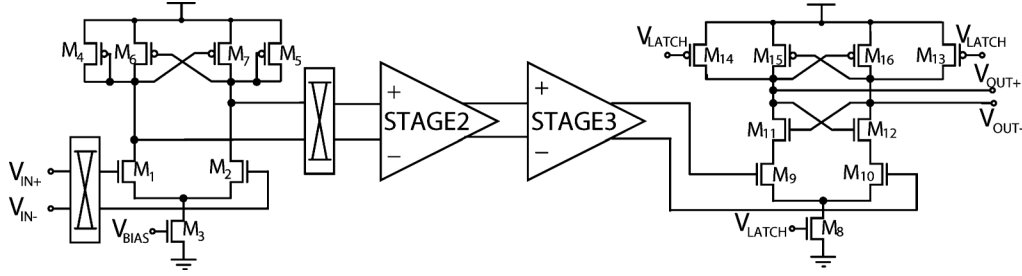


Fig. 12. High-speed latched comparator circuit schematic diagram.

TABLE I  
ADC COMPARATOR TRANSISTOR SIZING

Transistor	W/L ( $\mu\text{m}$ )	Transistor	W/L ( $\mu\text{m}$ )
$M_{1,2}$	24/1	$M_{9,10}$	3/0.4
$M_3$	2/4	$M_{11,12}$	36/0.5
$M_{4,5}$	4/1	$M_{13,14}$	6/4
$M_{6,7}$	8/1	$M_{15,16}$	36/0.5
$M_8$	4/4	—	—

recording channel. The output noise originates from the OTA, the feedback transistors  $M_p$ ,  $M_n$  and the regulated cascode output current mirror as shown in Fig. 8. The sub-circuit in Fig. 9 (active during the positive current recording) includes these elements and is used for noise analysis to simplify the derivation.

The impedance between the reference and working electrodes is modeled with a generic  $R$ - $C$  biosensor impedance model shown in Fig. 9, left. In this model  $R_S$  (typical value of 1 M $\Omega$ ) represents the electrolyte resistance between the working and reference electrodes,  $C_{WE}$  (typical value of 500 pF) represents the diffusion layer capacitance, and  $C_{DB}$  (typical value of 300 pF) models the interfacial double-layer capacitance at the WE-electrolyte interface and  $R_{CT}$  (typical value of 1 G $\Omega$ ) models the charge transfer resistance at the WE-electrolyte interface [16]. The input-referred noise of the OTA is due to its thermal and flicker noise. Both noise sources can be referred to the positive input of the OTA and are modeled as the voltage source  $V_n$  in Fig. 9 [56].

According to the simplified model given in Fig. 9, the output noise power of the current conveyer is given by

$$\begin{aligned}
 I_{n,OUT}^2 = & \beta_1 \left( \left| \frac{g_{mp}A}{1 + g_{mp}AZ} \right|^2 \overline{V_n^2} + \left| \frac{1}{1 + g_{mp}AZ} \right|^2 I_{np}^2 \right) \\
 & + I_{n,18}^2 + I_{n,15}^2 + g_{m18}^2 \left( \beta_2 \left( \left| \frac{g_{mp}A}{1 + g_{mp}AZ} \right|^2 \overline{V_n^2} \right. \right. \\
 & \left. \left. + \left| \frac{1}{1 + g_{mp}AZ} \right|^2 I_n^2 \right) + I_{n,13,14,16,17,18,19,20}^2 \right) \quad (1)
 \end{aligned}$$

where  $V_n^2$  is the OTA input-referred noise,  $I_{np}^2$  is the noise due to the feedback transistor  $M_p$ ,  $g_{mp}$  is the transconductance of

the PMOS feedback transistor  $M_p$ ,  $A$  is the open-loop gain of the OTA and  $Z$  is the equivalent impedance of the electrode.  $\beta_1$  and  $\beta_2$  are the current mirror ratios between the transistors  $M_{12}$ ,  $M_{13}$  and  $M_{12}$ ,  $M_{15}$ , respectively. In this design both ratios are set to one.

For practical values of  $g_{mp}$ ,  $A$  and  $Z$ , the contribution of  $I_{np}^2$  in (1) is negligible, resulting in the total output current noise

$$\begin{aligned}
 I_{n,OUT}^2 \approx & \beta_1 \left( \left| \frac{1}{Z} \right|^2 \overline{V_n^2} \right) + I_{n,18}^2 + I_{n,15}^2 \\
 & + g_{m18}^2 \left( \beta_2 \left( \left| \frac{1}{Z} \right|^2 \overline{V_n^2} \right) + I_{n,13,14,16,17,18,19,20}^2 \right). \quad (2)
 \end{aligned}$$

Since the electrolyte resistance,  $R_S$ , is typically small, and the charge transfer resistance,  $R_{CT}$ , is very large, the electrode equivalent impedance is approximately capacitive

$$Z \approx \frac{1}{j\omega(C_{WE} + C_{DB})} \quad (3)$$

where  $C_{WE}$  represents the diffusion layer capacitance and  $C_{DB}$  models the interfacial double-layer capacitance at the WE-electrolyte interface as shown in Fig. 9. Substituting (3) into (2) results in

$$\begin{aligned}
 I_{n,OUT}^2 \approx & \beta_1 \left( |2\pi f(C_{WE} + C_{DB})|^2 \overline{V_n^2} \right) + I_{n,18}^2 + I_{n,15}^2 \\
 & + g_{m18}^2 \left( \beta_2 (|2\pi f(C_{WE} + C_{DB})|^2 \overline{V_n^2}) \right. \\
 & \left. + I_{n,13,14,16,17,18,19,20}^2 \right). \quad (4)
 \end{aligned}$$

According to (4), the output noise level is proportional to the input-referred noise of the OTA as shown in Fig. 9, the current noise contributions from the regulated cascode current mirror transistors and the electrode capacitance. The electrode capacitance is determined by the electrode surface area. In general the larger the area of the electrode the more biomolecules there are to undergo a redox reaction resulting in a larger input signal. As a result, the electrode size and thus capacitance do not affect the SNR of the electrochemical recording system significantly. The input-referred noise of the OTA consists of two components, the

thermal noise power and the  $1/f$  noise. The thermal noise component can be expressed as [56]

$$\frac{\overline{V_{n,thermal}^2}}{\Delta f} = \frac{4KT}{g_{m1}} \left( \frac{4}{3} \right) \left( 1 + \frac{g_{m3}}{g_{m1}} + \frac{g_{m9}}{g_{m1}} \right) \quad (5)$$

where  $K$  is the Boltzmann constant and  $T$  is the absolute temperature. The noise contribution of  $M_{3,4,9,10}$  is minimized by biasing  $M_{3,4,9,10}$  such that  $g_{m3,4,9,10} \ll g_{m1,2}$ . The key to minimize the  $g_m$  ratios is to bias the input differential pair transistors in the weak inversion region, where the transconductance efficiency,  $g_m/I_D$ , is high, and to bias  $M_{3,4,9,10}$  in the strong inversion region to lower their  $g_m$ .

The input-referred  $1/f$  noise power can be expressed as [56]

$$\frac{\overline{V_{n,1/f}^2}}{\Delta f} = \frac{2K_P}{C_{OX}W_1L_1f} + \frac{2K_N}{C_{OX}W_3L_3f} \left( \frac{g_{m3}}{g_{m1}} \right)^2 + \frac{2K_P}{C_{OX}W_9L_9f} \left( \frac{g_{m9}}{g_{m1}} \right)^2 \quad (6)$$

where  $C_{OX}$  is gate oxide capacitance per unit area. In order to minimize the  $1/f$  noise, large PMOS input-pair transistors, long-channel current mirrors and internal OTA chopping are employed.

The noise contribution of the output regulated cascode current mirror is mostly governed by the transistors transconductance. The channel noise of a transistor is given by [56]

$$I_n^2 = 4KT \left( \frac{2}{3} \right) g_m + \frac{K}{WLC_{OX}f} g_m. \quad (7)$$

Thus, the  $g_m$  of the current mirror transistors should be reduced and the length of the transistor should be increased in order to reduce the current mirror noise contribution to the output of the current conveyer.

The simulated input-referred noise of the current conveyer for the cases where the chopper is disabled and enabled is shown in Fig. 10. The electrode model shown in Fig. 9 was included in the noise simulation to model the effect of the voltage ripple and the leakage current [54]. In this simulation  $R_S$  was set to 1 M $\Omega$ ,  $C_{WE}$  was set to 500 pF,  $C_{DB}$  was set to 300 pF and  $R_{CT}$  was set to 1 G $\Omega$ . This takes into account the effect of the high sensor output impedance on the noise performance of the chopper. The integrated input-referred noise from 0.01 Hz to 1 kHz is 0.27 pA for the case when the chopper is disabled and is 0.13 pA when the chopper is enabled.

The chopper implementation yeilds an 8 dB improvement in the noise floor with the realistic high-impedance electrode model. Off-chip access to the analog output of the current conveyer is not aviable, and as a result, the noise can not be measured directly before the quantization noise is added. The dual-slope ADC integrates the output current of the current conveyer in every ADC conversion cycle. This integration significantly reduces the effect of the ripples caused by chopper switches on the output of the current recording channel. Also, given that the chopper is implemented inside the OTA (internal OTA chopping) the limited bandwidth of the OTA combined with the 2

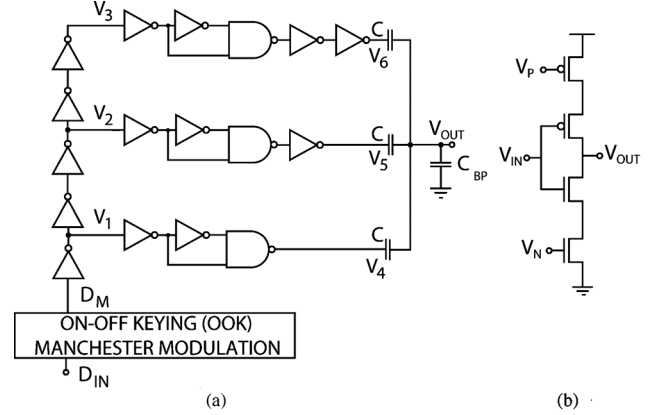


Fig. 13. (a) Ultra-wideband transmitter circuit schematic diagram, and (b) schematic of one current-starved inverter.

pF integrating capacitor, shown in Fig. 7, act as a low-pass filter thus further reducing the ripple levels.

The contribution of each transistor to the total input-referred noise is shown in Fig. 11. When the chopper is disabled the main contributions are from the OTA current mirror transistors  $M_{3,4}$  and the input pair transistors  $M_{1,2}$ . When the chopper is enabled, the current mirror transistors  $M_{12,21,24,15}$  are the main contributors to the input-referred noise.

### C. Dual-Slope ADC Comparator

The ADC comparator is implemented with three stages of pre-amplifiers, with a total gain of 60 dB and the last stage with a high-speed latch as shown in Fig. 12. The first stage of the comparator is implemented as a cross-coupled diode-connected gain stage. This topology provides a moderate gain and a high frequency bandwidth. Chopper-stabilization suppresses the input offset and ensures 9-bit accuracy. The second and third stages are identical to the first one but with no chopping. The high-speed latch is implemented with an NMOS input pair gain stage and a NMOS-PMOS cross-coupled load. This topology provides high accuracy, low offset and a high frequency bandwidth. The comparator transistor sizes are listed in Table I.

### D. Ultra-Wideband Transmitter

The circuit diagram of the all-digital pulsed UWB transmitter is shown in Fig. 13(a). The input data are modulated using on-off keying (OOK) Manchester modulation. UWB pulses are generated on the rising edge of the modulated data ( $D_M$ ). A delay line bank is employed together with a capacitively coupled output combiner [49] as shown in Fig. 13(a). The modulated data are passed through a delay line, and a delayed version of the data are passed through three pulse generators. The pulse generators shape a first-order Gaussian pulse at the rising edge of the input data. The presented digital UWB transmitter achieves both power efficiency and spectral compliance in a much smaller chip area compared to earlier designs [50], [51].

As illustrated in Fig. 14, each pulse generator forms pulses that are delayed, and have opposite signs. By capacitively combining the three paths, the opposite signs are canceled, and the zero-DC double-differentiated Gaussian pulse propagates to the

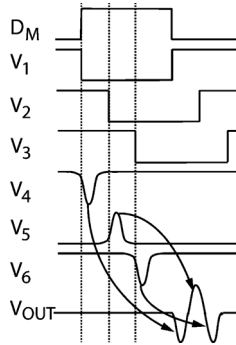


Fig. 14. Timing diagram of the ultra-wideband transmitter.

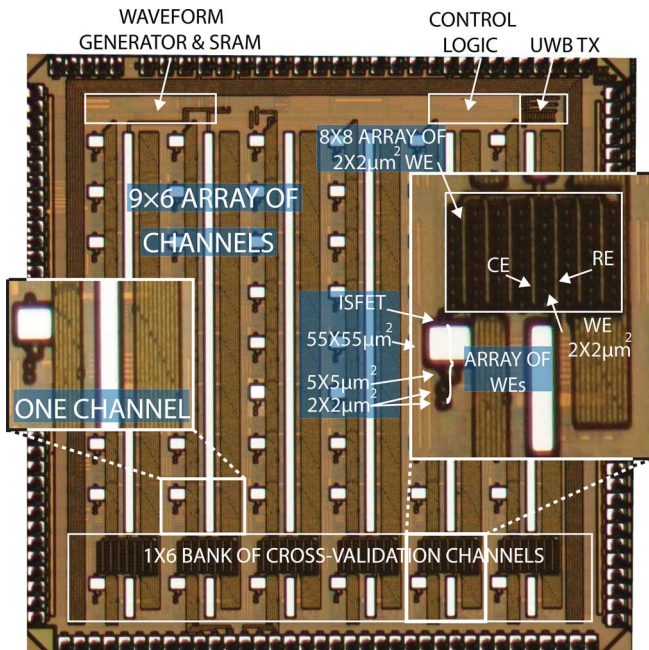


Fig. 15. Die micrograph of the 3 mm × 3 mm 54-channel wireless DNA analysis SoC. The SoC was fabricated in a 0.13  $\mu\text{m}$  standard CMOS technology.

single-ended antenna [50], [51]. The width of the output pulse depends on the delays in the delay line. The delay cells in all the paths are implemented as current-starved inverters, shown in Fig. 13(b), to allow for tuning of the UWB pulse width.

## VI. ELECTRICAL EXPERIMENTAL RESULTS

The fabricated prototype die micrograph is depicted in Fig. 15. The 54 channels are arranged in a 9 × 6 array on a 3 mm × 3 mm 0.13  $\mu\text{m}$  CMOS die. Two channel types with two different WE aluminum base configurations are implemented. A set of 48 channels of the first type scan 4 WEs each, in order to perform initial detection of DNA. They have three different WE aluminum base sizes of 2  $\mu\text{m}$  × 2  $\mu\text{m}$  (twice), 5  $\mu\text{m}$  × 5  $\mu\text{m}$  and 55  $\mu\text{m}$  × 55  $\mu\text{m}$  each as needed to cover a wide combined dynamic range. An additional set of 6 channels of the second type (at the bottom of the array in Fig. 15) additionally scan a sub-array of 8 × 8 2  $\mu\text{m}$  × 2  $\mu\text{m}$  WEs each.

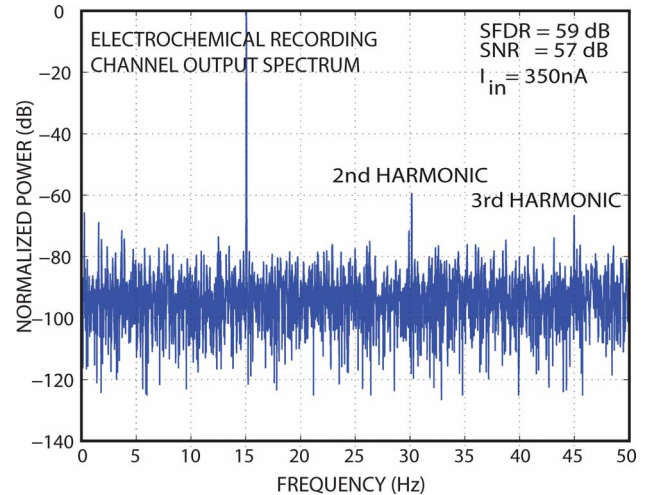


Fig. 16. Experimentally measured spectrum of the electrochemical recording channel output for a 15 Hz sinusoidal full-scale (350 nA) input.

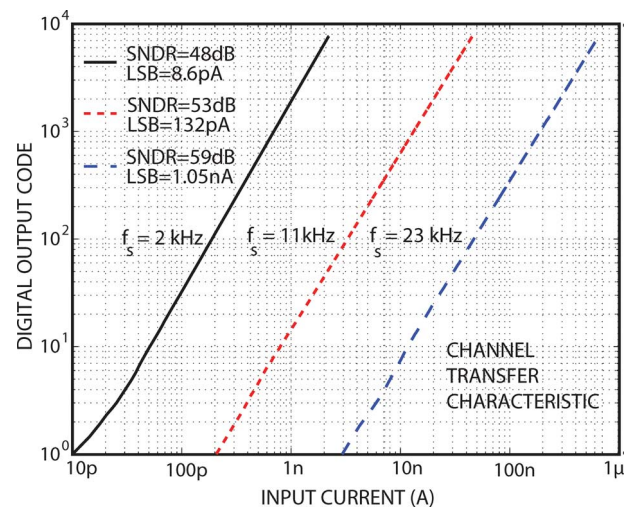


Fig. 17. Experimentally measured transfer characteristics of the current-to-digital channel for three sampling frequencies.

These redundant-electrode sub-arrays are utilized for DNA detection results cross-validation and for titer DNA concentration measurements.

Dynamic performance of the entire channel was measured by applying a 15 Hz full-scale (350 nA) sinusoidal input current sampled at 23 kHz. Fig. 16 shows the 65536-point FFT of the measured ADC output. The strong second harmonic is due to the single-ended nature of the architecture of the ADC. The resulting effective number of bits (ENOB) is 9.1.

For static performance characterization the input DC current of one typical channel was swept between 10 pA and 350 nA as shown in Fig. 17. The input dynamic range is 93 dB cumulatively for the three sampling frequency settings, or 48 dB at one fixed sampling frequency of 2 kHz. The dynamic range for each setting is computed by taking the ratio of the maximum signal that saturates the ADC to the LSB for a given sampling frequency setting.

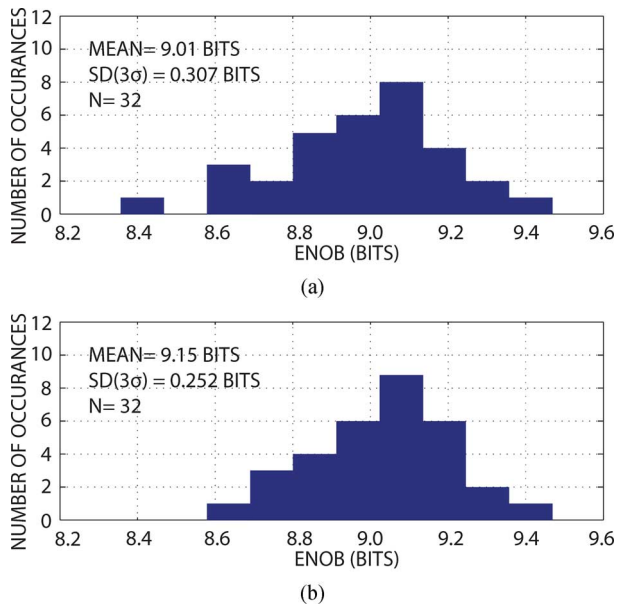


Fig. 18. Experimentally measured output ENOB of 32 channels (from 16 chips, two channels each) for a 15 Hz 350 nA sinusoidal input (a) without calibration, and (b) with in-channel calibration.

Two sets of ENOB measurements were conducted to study the effectiveness of the in-channel gain calibration using the in-channel SRAM to adjust the ADC timing. In the first measurement no calibration has been performed and the timing parameters of all channels are set to a constant value (all the ADCs have the same charging and discharging phases duration). Fig. 18(a) shows the experimentally recorded ENOB for a 15 Hz full-scale (350 nA) sinusoidal input current from 32 channels on 16 chips (two channels per chip), with the ADC clocked at 12 MHz. The mean ENOB and the corresponding standard deviation are 9.01 and 0.307 respectively. Next, the same set of experiments were repeated with the calibrated channels, as described at the end of Section IV-B. Fig. 18(b) shows the experimentally recorded ENOB for the same input tone as the previous case. The mean ENOB and the corresponding standard deviation are 9.15 and 0.252, respectively. The calibration improves the ENOB standard deviation by 17%.

Fig. 19 shows the ADC ENOB versus the frequency for a full-scale (350 nA) sinusoidal input current. The ADC maintains an ENOB of greater than 8.5 bits at up to 3.4 kHz. The drop in the ENOB is due to the limited bandwidth of the front-end current conveyor and high-frequency switching interference noise.

The experimentally measured relative errors of the digital output for the input current swept between  $\pm 10$  pA and  $\pm 350$  nA are shown in Fig. 20. The relative error stays below 6% over the whole operating range. This is an improvement of 33% compared to the design without the DEM [54]. Fig. 20 illustrates an improvement in the output relative error of approximately 25% due to the use of DEM in this design as compared to a previously reported design without DEM [54]. The current conveyor achieves a dynamic range of 8.6 pA to 350 nA or 93 dB. The lower limit is defined by the ADC LSB and the higher limit is defined by the input current that saturates the current conveyor.

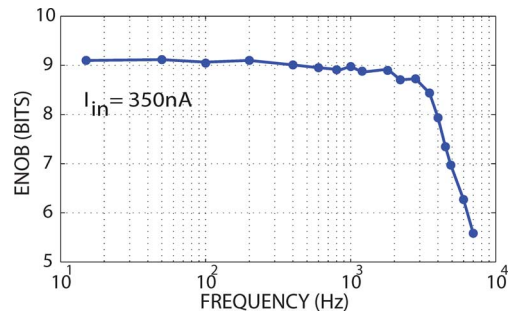


Fig. 19. Experimentally measured ENOB vs. input frequency for the in-channel ADC.

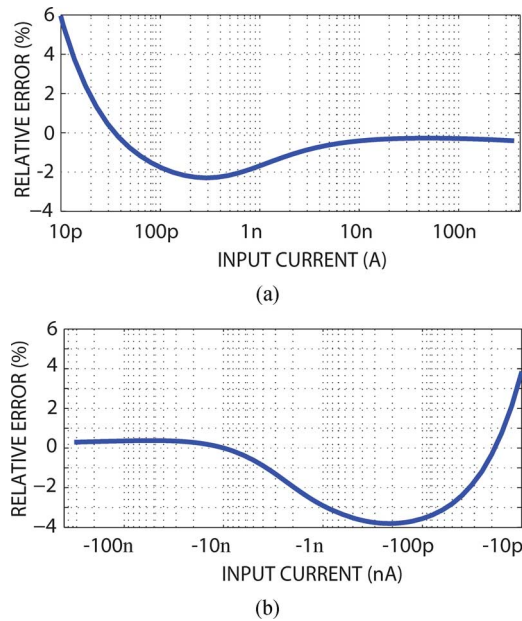


Fig. 20. Experimentally measured relative error of the output digital code of the current conveyor connected with the dual-slope ADC for (a) 10 pA to 350 nA and (b)  $-350$  nA to  $-10$  pA input current.

Fig. 21 shows the experimentally recorded output current distribution for the input current of 100 pA measured from 32 channels on 16 chips (two channels per chip) without dynamic element matching [54] and with dynamic element matching implemented in this design. The mean output current and the corresponding standard deviation without dynamic element matching [54] are 81.26 pA and 20.2 pA, respectively. In this design, with dynamic element matching added, they are 92.12 pA and 9.2 pA, respectively. Adding DEM results in a 54% improvement in channel-to-channel accuracy.

As shown in Fig. 22 the same experiment is repeated with the input current level of 100 nA. The mean output current and the corresponding standard deviation without dynamic element matching [54] are 100.26 nA and 34 pA, respectively. In this design, with dynamic element matching added to the design, they are 100.18 nA and 22 pA, respectively. Adding DEM results in a 35% improvement in channel-to-channel accuracy.

The input Manchester-encoded data to the UWB transmitter and its measured output UWB pulses are shown in Fig. 23.

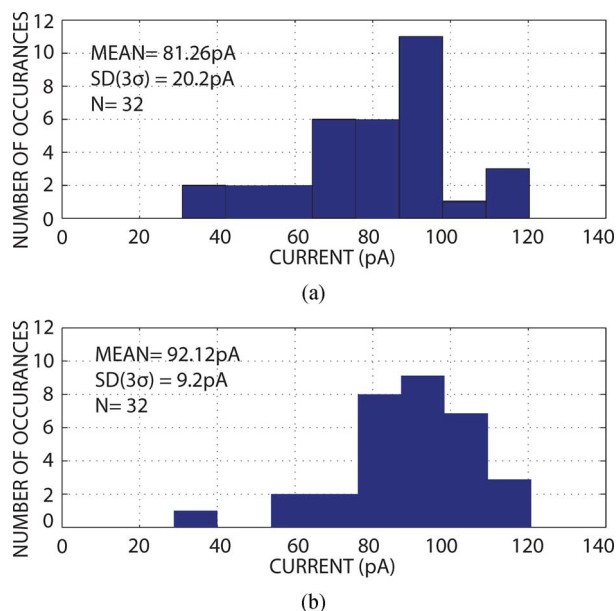


Fig. 21. Experimentally measured output current of 32 channels (from 16 chips, two channels each) for the input current of (a) 100 pA without DEM [32] and (b) 100 pA with DEM (this work).

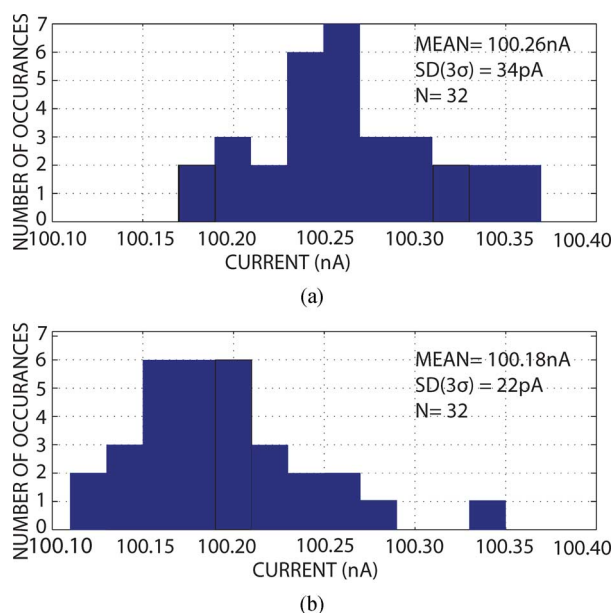


Fig. 22. Experimentally measured output current of 32 channels (from 16 chips, two channels each) for input current of (a) 100 nA without DEM [32] and (b) 100 nA with DEM (this work).

The UWB pulses are measured using custom-built UWB antennas (5 cm spacing between the transmitter and receiver) and a custom-built receiver. A zoomed-in version of one such the measured UWB pulse overlaid on a simulated UWB pulse is shown in Fig. 24. As it can be seen the measured pulse resembles the expected UWB pulse but includes minor ringing due to the package bondwire inductance. The measured output power spectrum of the UWB transmitter is plotted in Fig. 25. The power spectrum complies with the FCC-defined 0–1 GHz UWB spectrum (mask) also shown. An example of the input

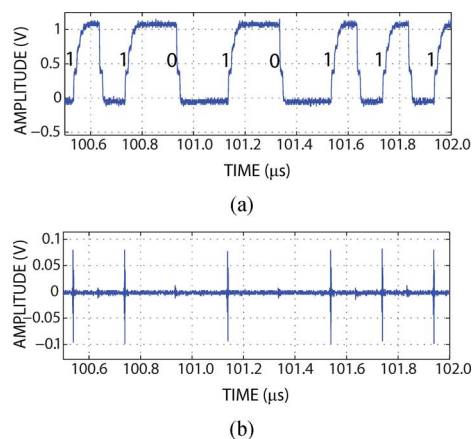


Fig. 23. Experimentally measured (a) Manchester-encoded input data to the UWB transmitter and (b) the output pulses.

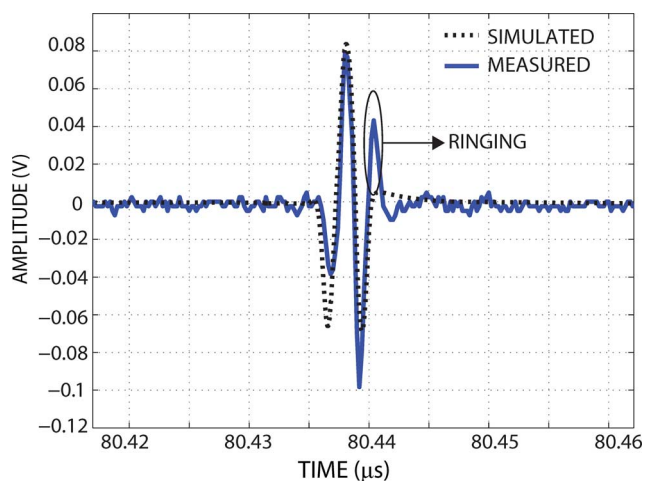


Fig. 24. Wirelessly measured UWB pulse at the distance of 5 cm using a custom-built UWB receiver.

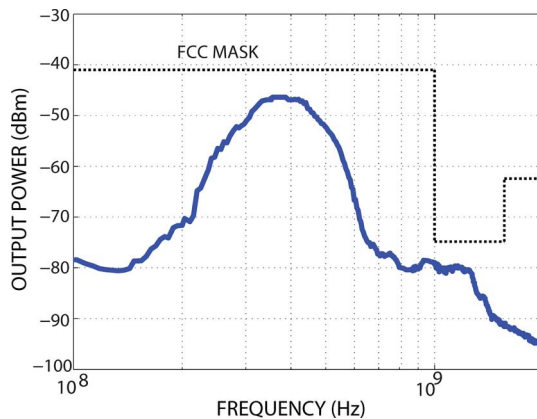


Fig. 25. Experimentally measured UWB transmitter output spectrum (direct output of the transmitter driving a 50 ohm load). The output spectrum is compliant with the 0–1 GHz FCC UWB band output power criteria.

data to the UWB transmitter Manchester-encoded at the rate of 10 Mb/s and the data received at the distance of 5 cm using a custom-built UWB receiver is shown in Fig. 26.

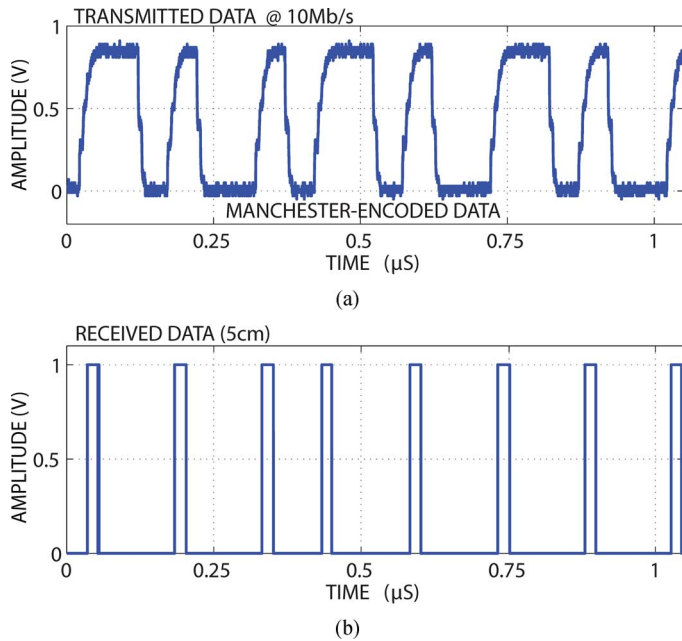


Fig. 26. (a) Manchester-encoded input data to the UWB transmitter and (b) the corresponding data received wirelessly at a 5 cm distance.

TABLE II  
EXPERIMENTALLY MEASURED ELECTRICAL CHARACTERISTICS

Technology	0.13 $\mu\text{m}$ CMOS
Supply Voltage	1.2V
Area	3mm $\times$ 3mm
Array Dimensions	9 $\times$ 6 channels
Channel Size	200 $\mu\text{m}$ $\times$ 300 $\mu\text{m}$
Sensitivity	8.6 pA
Power Consumption (System)	
Waveform Generator	1.1 mW
SRAM	1.3 $\mu\text{W}$
UWB Transmitter	400 $\mu\text{W}$
Power Consumption (Channel)	
Current Conveyor	8 $\mu\text{W}$
Comparator	19 $\mu\text{W}$
Biasing	4 $\mu\text{W}$
Digital	11 $\mu\text{W}$
Total (channel)	42 $\mu\text{W}$

Table II provides a summary of experimentally measured characteristics of the integrated CMOS DNA analyzer SoC.

## VII. EXPERIMENTAL ELECTROCHEMICAL RESULTS

To validate the performance of the channel in electrochemical sensing applications, CV, first, scans of a DNA reporter potassium ferricyanide and a buffer solution were performed. Potassium ferricyanide  $\text{K}_4[\text{Fe}(\text{CN})_6]$  is commonly used in electrochemical DNA detection systems as a redox reporter. Cyclic voltammetry recordings of 20  $\mu\text{M}$  potassium ferricyanide solution and 1 M potassium phosphate buffer (pH 7.3) have been carried out. On-chip waveform generator was utilized to generate the CV excitation waveform. A 500 mV//sec 0.7 V peak-to-peak ramp-up-ramp-down CV waveform with a 50 ms resting period was applied between a 55  $\mu\text{m}$   $\times$  55  $\mu\text{m}$  flat gold working electrode in Fig. 5(b) and an off-chip Ag/AgCl reference electrode (Basi, RE-5B). The resulting CV curves recorded by the chopper-stabilized channel with DEM are shown in Fig. 27. The phosphate buffer CV curve occurs mainly because of the charging and discharging of the electrode-electrolyte double layer capacitance and thus has no

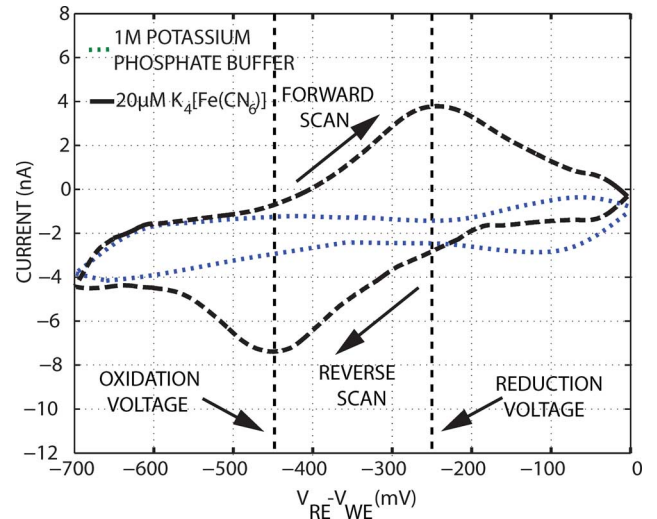


Fig. 27. Experimentally recorded cyclic voltammograms of 1 M potassium phosphate buffer and 20  $\mu\text{M}$  potassium ferricyanide solution using the 55  $\mu\text{m}$   $\times$  55  $\mu\text{m}$  working electrode in Fig. 5(b).

peak. In contrast, the potassium ferricyanide CV curve shows two distinct peaks at the reduction and oxidation voltages of potassium ferricyanide. Indeed, such flat electrodes, typically produce such distinct redox peaks.

The recorded CV waveforms characteristics (redox peaks location and spacing) are similar to those reported in the literature [40], [41]. A typical CV curve is shown in Fig. 2(b). The separation between the two peak potentials,  $\Delta E_p = E_{pc} - E_{pa}$ , can be used to determine the electrochemical reversibility for a redox couple. For a reversible CV reaction one has [55]

$$\Delta E_p = \frac{0.058}{n} \quad (8)$$

where  $n$  is the number of electrons transferred between the redox complex. This value is independent of the scan rate for fast electron transfer. Increasing values of  $\Delta E_p$  as a function of increasing scan rate indicates the presence of electrochemical irreversibility. In practice, the theoretical value of 58/ $n$  mV for  $\Delta E_p$  is seldom observed. In all experiments the potassium ferrocyanide solution was diluted in 1 M potassium phosphate buffer. This combined with the slow electron transfer kinetics present in case of our complex multi-material electrodes have caused the peak voltage difference to deviate from the theoretical 58 mV value [33], [34]. In all experiments, the first four CV curves were discarded and the fifth curve was used as the recorded data. As a result, the peak recorded redox current is consistent for different concentrations. Other recordings [33], [34] using a similar DNA detection method also achieve  $\Delta E_p$  higher than the theoretical value of 58 mV.

Next, CV scans of a potassium ferricyanide solution with four different concentrations (10  $\mu\text{M}$  to 40  $\mu\text{M}$ ) using a 55  $\mu\text{m}$   $\times$  55  $\mu\text{m}$  flat gold working electrode shown in Fig. 5(b) have been performed to study the effect of a change in the DNA reporter concentration on the recorded redox current. As shown in Fig. 28, the peak current at the reduction and oxidation voltages of potassium ferricyanide increases with an increase in its concentration. The corresponding calibration curve is shown

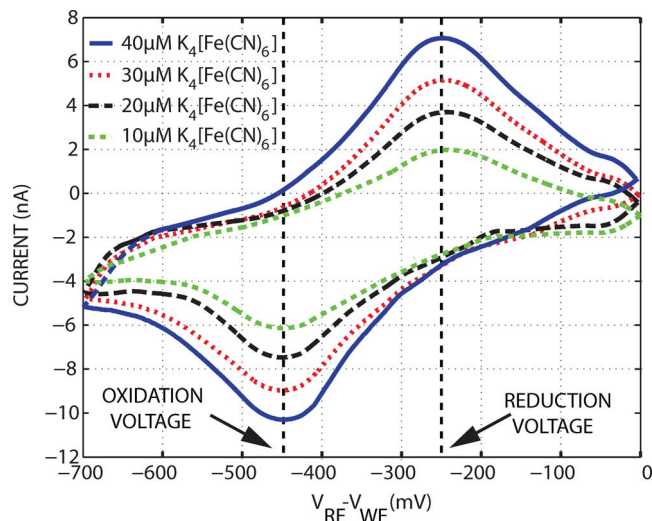


Fig. 28. Experimentally recorded cyclic voltammograms of 10  $\mu\text{M}$ , 20  $\mu\text{M}$ , 30  $\mu\text{M}$  and 40  $\mu\text{M}$  potassium ferricyanide solution using the 55  $\mu\text{m} \times 55 \mu\text{m}$  working electrode in Fig. 5(b).

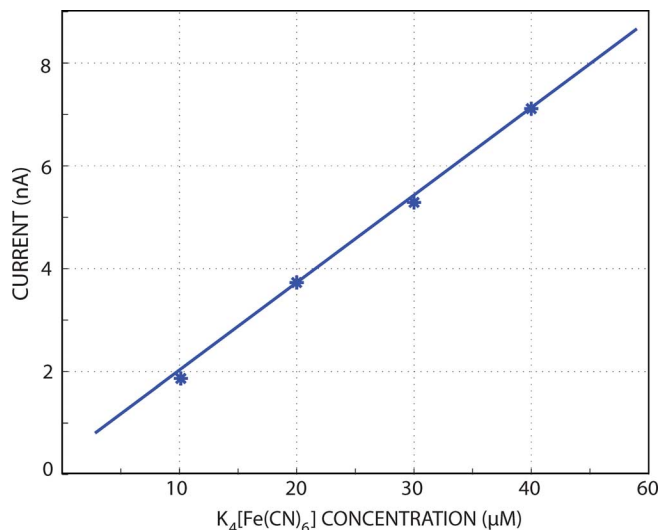


Fig. 29. Calibration curve for the peak reduction current of potassium ferricyanide solution for the 55  $\mu\text{m} \times 55 \mu\text{m}$  Au working electrode in Fig. 5(b).

in Fig. 29. This curve demonstrates the linear relationship between the concentration of potassium ferricyanide and the output redox current.

CV scans of a potassium ferricyanide solution at 40  $\mu\text{M}$  have been conducted on all 48 channels with 55  $\mu\text{m} \times 55 \mu\text{m}$  flat gold working electrodes shown in Fig. 5(b) to study the effect of the channel-to-channel variation on the CV recording results. A 500 mV/sec 0.7 V peak-to-peak ramp-up-ramp-down CV waveform with a 50 ms resting period was used in this experiment. Fig. 30 shows the resulting peak reduction currents recorded by the 48 channels. The mean peak reduction current is 7.02 nA, and the three-sigma variation is 0.22 nA.

To validate the performance of the pH sensors, the sensitivity of the ISFET is measured in response to change in the solution pH level. A preliminary analysis of the ISFET characteristics indicated that the pH sensors have different threshold voltages, due to the trapped charge on the floating gates of the ISFETs.

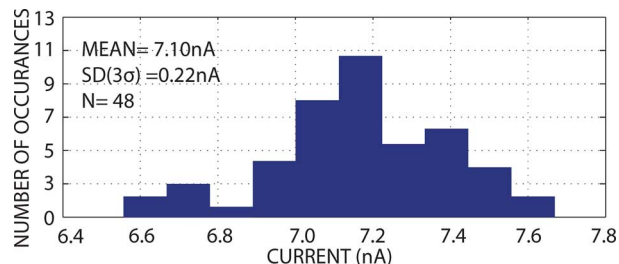


Fig. 30. Experimentally recorded peak reduction current of the 40  $\mu\text{M}$  potassium ferricyanide solution recorded using the 55  $\mu\text{m} \times 55 \mu\text{m}$  working electrode shown in Fig. 5(b) by 48-channel on the CMOS DNA analysis SoC.

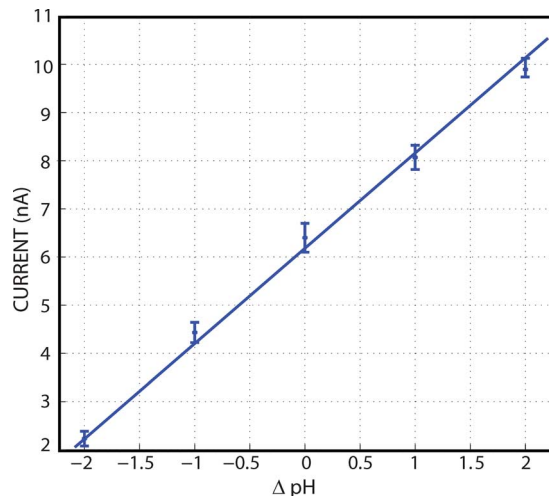


Fig. 31. Experimentally measured on-chip pH sensor calibration curve relative to pH of 7. A total of 60 measurements from 3 chips, 20 measurements each, have been performed. The corresponding 3 $\sigma$  error bars are shown.

The UV radiation and bulk substrate biasing (for 8 hours) technique was used to remove the trapped charge and thus remove the threshold voltage mismatch among the pH sensors. Before the pH sensor sensitivity is measured, the sensor array must be etched for 10 s in a 10% buffered hydrofluoric acid solution. Measurements made without this step are generally very noisy and result in a low sensitivity. After the threshold voltage calibration, the sensitivity of the pH sensor is measured in a 0.1 M NaCl electrolyte by adding small quantities of hydrochloric acid to change the solution pH from five to nine. Recording the calibrated steps in the measured current leads to the finding that the array has a linear response of 1.8 nA/pH. The corresponding calibration curve with error bars (from three chips, 20 measurements each) is shown in Fig. 31.

## VIII. SYNTHETIC PROSTATE CANCER DNA DETECTION

The SoC has been validated in label-free amperometric detection of synthetic prostate cancer DNA. The DNA sequences are synthesized by Integrated DNA technology [57]. The following synthetic DNA sequences have been used in the experiments: DNA probes (5ThioMC6-D/AG CGC GGC AGG AAG CCT TAT), complementary target DNA (ATA AGG CTT CCT GCC GCG CT) and non-complementary DNA (TTT TTT TTT TTT TTT TTT TT). All the DNA experiments were conducted at room temperature. In all the experiments a 500 mV/sec 0.7 V peak-to-peak ramp-up-ramp-down CV waveform with a 50 ms

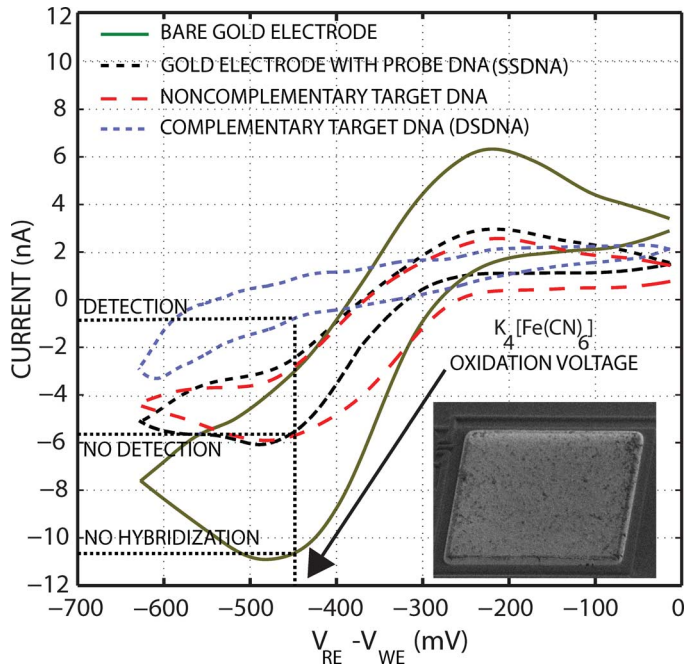


Fig. 32. Experimentally measured cyclic voltammetry results of 5  $\mu\text{M}$  prostate cancer synthetic DNA detection from the 55  $\mu\text{m} \times 55 \mu\text{m}$  flat gold working electrode in Fig. 5(b).

resting period was applied between the working electrode and a commercially available off-chip Ag/AgCl reference electrode (Basi RE-5B) [58].

Fig. 32 shows cyclic voltammetry scans from an on-chip 55  $\mu\text{m} \times 55 \mu\text{m}$  flat gold electrode for the 5  $\mu\text{M}$  prostate cancer synthetic DNA cyclic voltammetry recording, in a 40  $\mu\text{M}$  potassium ferricyanide solution. The CV scan rate and range were set to 500 mV/sec and 0.7 V peak-to-peak, respectively, with a 40 ms resting period. The bare gold electrode CV scan demonstrates well-defined oxidation and reduction peaks, whereas scans taken using 5  $\mu\text{M}$  single-stranded probe DNA attached to electrodes show a reduction in the oxidation/reduction peaks. This is expected since thiolated DNA probes create a negatively charged film on the electrode repelling the negatively charged electrochemical reporter potassium ferricyanide as illustrated in Fig. 3. Further adding a 5  $\mu\text{M}$  non-complementary DNA target does not change the CV signal oxidation peak value significantly indicating that non-specific adsorption is negligible. On the other hand, adding a 5  $\mu\text{M}$  complementary target single-stranded DNA onto the chip leads to creation of double-stranded DNA on the biosensing electrode resulting in an additional negative charge and elimination of potassium ferricyanide redox peaks. The corresponding error bars (from 3 chips, 20 measurements each) are shown in Fig. 33. As it can be seen, the detectible signal change in this case is 2.85 nA.

The same set of experiments were repeated with the on-die nanostructured electrodes to study their DNA detection capabilities. Fig. 34 shows the CV curves obtained for a nanostructured electrode grown at  $V_{RE} - V_{WE} = 0$  mV for 100 aM prostate cancer synthetic DNA concentration, in a 40  $\mu\text{M}$  potassium ferricyanide solution. As expected, compared to the flat gold electrodes the nanostructured electrodes typically do not

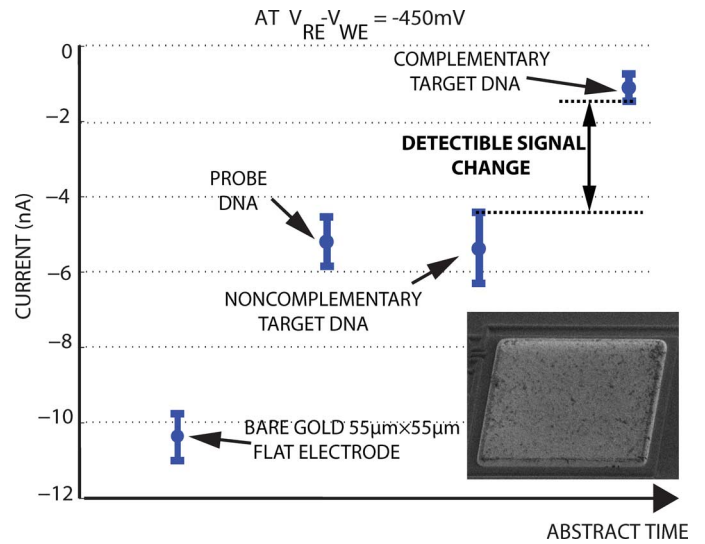


Fig. 33. Experimentally measured 5  $\mu\text{M}$  prostate cancer synthetic DNA cyclic voltammetry recording  $3\sigma$  error bars from 3 chips 60 measurements each from 55  $\mu\text{m} \times 55 \mu\text{m}$  flat gold working electrodes in Fig. 5(b).

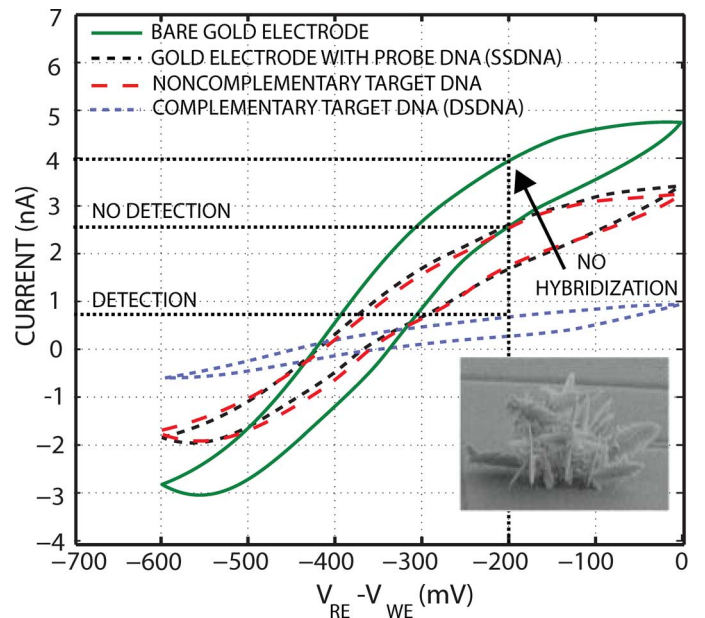


Fig. 34. Experimentally measured cyclic voltammetry results of 100 aM prostate cancer synthetic DNA detection, from 2  $\mu\text{m} \times 2 \mu\text{m}$  nanostructured working electrodes in Fig. 4(e).

exhibit the redox peaks [37]. As it can be seen from Fig. 34 the current level in the presence of complementary target DNA (DSDNA) is smaller compared to the case where only the probe DNA (SSDNA) is present. The corresponding error bars (from 3 chips, 60 measurements each) are shown in Fig. 35. As it can be seen, the detectible signal change in this case is 1.1 nA.

DNA sensing experiments were conducted for the target DNA concentrations of 1 aM to 10  $\mu\text{M}$  to study the detection limits of the on-die nanostructured electrodes and the on-die flat gold electrode. The resulting characteristics, detection limits and dynamic ranges of the two nanostructured electrode types and the 55  $\mu\text{m} \times 55 \mu\text{m}$  flat gold electrode are given in Fig. 36.  $\Delta I$  is computed as  $(I_{DSDNA} - I_{SSDNA})/I_{SSDNA} \times 100$ ,

TABLE III  
COMPARATIVE ANALYSIS OF AMPEROMETRIC SENSORY MICROSYSTEMS

System	ISSCC 08 [33]	JSSC 08 [34]	JSSC 09 [16]	ISSCC 10 [18]	ISSCC 10 [35]	This Work
<b>Technology (CMOS)</b>	0.18 $\mu\text{m}$	0.25 $\mu\text{m}$	0.5 $\mu\text{m}$	0.35 $\mu\text{m}$	0.6 $\mu\text{m}$	0.13 $\mu\text{m}$
Power	25mW	160mW	0.6mW	84.5mW	N/A	0.35mW
Supply Voltage	5.0V	2.5V	3.0V	3.3V	3.3V	1.2V
Chip Area	11.2mm <sup>2</sup>	15mm <sup>2</sup>	2.25mm <sup>2</sup>	4mm <sup>2</sup>	25.8mm <sup>2</sup>	9mm <sup>2</sup>
Electrode Count	576	54	100	100	40	600
<b>Channel</b>						
Sensing Protocol	CV	CV	IS	IS	CA	CV
Channel Count	24	16	100	100	40	54
Type of Electrodes	2D	2D	2D	2D	2D	2D Flat, 3D
	Polymer	Gold	Gold	Gold	pH	Nanostructured Gold
Power	N/A	10mW	6 $\mu\text{W}$	0.84mW	N/A	42 $\mu\text{W}$
Dynamic Range	N/A	60dB	58dB	N/A	50dB	93dB (3-mode)
Conversion Rate	10Hz	10kHz	10kHz	N/A	1Hz	10kHz
Sensitivity	97pA	240pA	10kHz	330pA	25 $\mu\text{V}$	8.6pA
ENOB	11 bits	9 bits	8 bits	No ADC	12 bits	9.1 bits
<b>Waveform Generator</b>	No	No	Yes	Yes	No	Yes
Type	—	—	Square Wave	Square Wave	—	8-bit Programmable
Frequency (Period)	—	—	10kHz	50MHz	—	10kHz
Power	—	—	—	—	—	1.1mW (5nF Load)
<b>Transmitter</b>	No	No	No	No	No	Yes
Protocol	—	—	—	—	—	0-1, 3-10.6 GHz UWB
Data Rate	—	—	—	—	—	10Mbps
Power	—	—	—	—	—	100 $\mu\text{W}$
<b>Sensors</b>						
Type	DNA	DNA	Protein	DNA	DNA	DNA
On-die	Yes	Yes	Yes	Yes	Yes	Yes
Label-free	No	Yes	No	No	No	Yes
PCR-free	No	No	No	No	Yes	Yes
Biomolecule Type	30 Base Pairs	18 Base Pairs	Bilayer Lipid Membrane	Bovine Serum Albumin	Single Nucleotide Polymorphisms	20 Base Pairs
Concentration	10nM-100nM	100nM	1 $\mu\text{M}$	100mM	N/A	10aM-10 $\mu\text{M}$

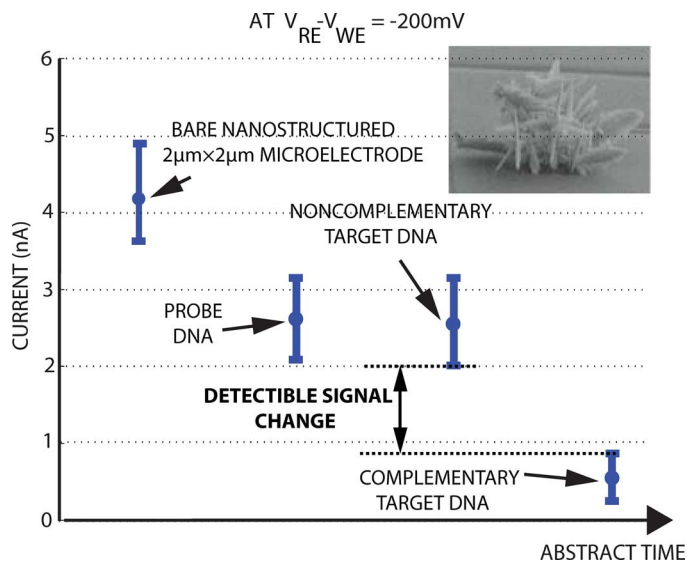


Fig. 35. Experimentally measured 100 aM prostate cancer synthetic DNA cyclic voltammetry recording  $3\sigma$  error bars from 3 chips, 60 measurements each, from  $2\mu\text{m} \times 2\mu\text{m}$  nanostructured working electrodes in Fig. 4(e).

where  $I_{DSDNA}$  is the redox current after the hybridization and  $I_{SSDNA}$  is the redox current before the hybridization. All the current recordings for nanostructured electrodes are taken at  $V_{RE} - V_{WE}$  of  $-200\text{ mV}$  and at  $V_{RE} - V_{WE}$  of  $-250\text{ mV}$  for the flat gold electrodes. The corresponding error bars (from 3 chips, 100 measurements each) are also shown in Fig. 36.

The detection limit, defined as the lowest concentration for which the background-subtracted signal is three times higher

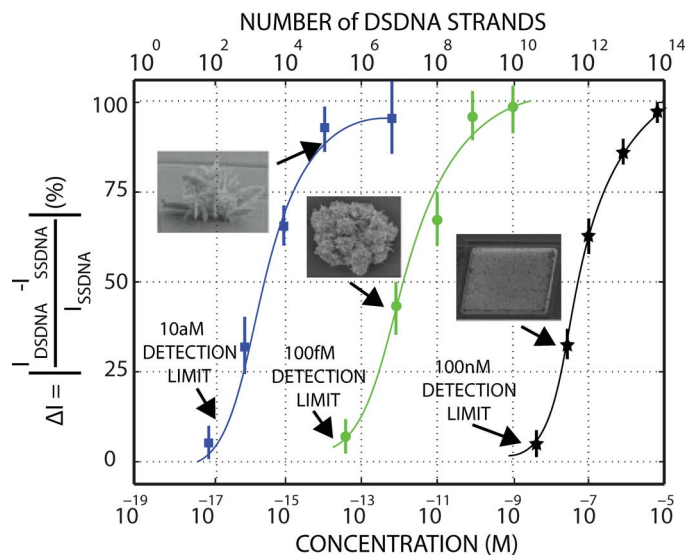


Fig. 36. Experimentally measured microelectrode characteristics, detection limits and dynamic ranges in prostate cancer synthetic DNA detection using the three electrodes types shown in Figs. 4(d) and (e) and 5(b). Error bars (3 sigma) are from 3 chips, 100 measurements each.

than the standard deviation at that concentration, for nanostructured electrodes grown at  $V_{RE} - V_{WE} = 0\text{ mV}$  as shown in Fig. 36 is 10 aM. The 10 aM sensitivity achieved using the optimized on-CMOS nanostructured electrode enables PCR-free detection for many applications. This limit corresponds to the detection of fewer than 100 copies of the target sequence.

Another benefit of having several types of electrodes on the same chip is that different electrodes cover different concentration ranges. As it can be seen from Fig. 36, the nanostructured electrodes grown at  $V_{RE} - V_{WE} = 0$  mV cover a dynamic range (defined as the range at which the 3 sigma error bar of the given concentration is below 100 and above 0 on the y-axis) of 3 aM to 100 fM, the nanostructured electrodes grown at  $V_{RE} - V_{WE}$  of 100 mV cover a dynamic range of 100 fM to 90 pM, and the  $55 \mu\text{m} \times 55 \mu\text{m}$  flat gold electrodes cover a dynamic range of 1 nM to 10  $\mu\text{M}$ . As a result, by fabricating electrodes with different degrees of nanostructuring, we can significantly expand the dynamic range of the CMOS DNA sensing microsystem (as wide as 140 dB with these types of nanostructured microelectrodes [37]).

Table III provides a comparative analysis of the presented design and existing amperometric biochemical sensory microsystems. The design presented in this work achieves the highest dynamic range and the lowest sensitivity in terms of ADC LSB. We have shown successful detection of 20-base pair long synthetic prostate cancer DNA from several types of on-chip Au electrodes. The 10 aM detection limit is the lowest detection limit reported in literature from an integrated circuit-based DNA sensor to date.

## IX. CONCLUSIONS

A 54-channel 0.13  $\mu\text{m}$  CMOS fast-scan cyclic voltammetry DNA analysis SoC has been presented. The microsystem includes 600 time-multiplexed DNA sensors and 54 pH sensors. It also includes an arbitrary waveform generator, an on-chip memory, an in-channel low-noise chopper-stabilized front-end current conveyer with dynamic element matching, an in-channel dual-slope ADC and a fully digital ultra-wideband transmitter. Chopper stabilization achieves input-referred noise of less than 0.13 pA over the operating bandwidth. Dynamic element matching improves current conveyer accuracy by 54% at the 100 pA input current level. The in-channel SRAM enables in-channel calibration which results in a 17% improvement in channel-to-channel ENOB variation. Each channel occupies an area of 0.06 mm<sup>2</sup> and consumes 42  $\mu\text{W}$  of power from a 1.2 V supply. The presented current-to-digital channel design achieves a combined dynamic range of 93 dB with the sensitivity of 8.6 pA. Two types of nanostructured microelectrodes and one type of a flat gold electrode have been characterized in on-CMOS DNA prostate cancer detection. The on-chip nanostructured microelectrodes achieve label-free PCR-free detection limit of 10 aM, which is the lowest reported on-CMOS detection limit.

## REFERENCES

- [1] B. A. Flusberg, D. R. Webster, J. H. Lee, K. J. Travers, E. C. Olivares, T. A. Clark, J. Korlach, and S. W. Turner, "Direct detection of DNA methylation during single-molecule, real-time sequencing," *Nature Methods*, vol. 7, pp. 461–465, 2010.
- [2] G. Liu, Y. Wan, V. Gau, J. Zhang, L. Wang, S. Song, and C. Fan, "An enzyme-based E-DNA sensor for sequence-specific detection of femtomolar DNA targets," *J. Amer. Chem. Soc.*, vol. 130, no. 21, pp. 6820–6825, 2008.
- [3] B. Malorny, C. Bunge, and R. Helmuth, "A real-time PCR for the detection of salmonella enteritidis in poultry meat and consumption eggs," *J. Microbiological Methods*, vol. 70, no. 2, pp. 245–251, 2007.

- [4] S. Cagnin, M. Caraballo, C. Guiducci, P. Martini, M. Ross, M. S. Ana, D. Danley, T. West, and G. Lanfranchi, "Overview of electrochemical DNA biosensors: New approaches to detect the expression of life," *Sensors*, vol. 9, no. 4, pp. 3122–3148, 2009.
- [5] A. Sassolas, B. D. Leca-Bouvier, and L. J. Blum, "DNA biosensors and microarrays," *Chemical Reviews*, vol. 108, pp. 109–139, 2008.
- [6] A. Nouri and C. F. Chyba, "DNA synthesis security," *Methods in Molecular Biol.*, vol. 8, no. 4, pp. 285–296, 2012.
- [7] B. Albert, A. Johanson, J. Lewis, M. Raff, K. Robert, and P. Walter, *Molecular Biology of the Cell*, 5th ed. New York, NY, USA: Garland Science, 2008.
- [8] M. Schena, *Mircorarray Analysis*. Hoboken, NJ, USA: Wiley, 2003.
- [9] O. A. Loaiza, S. Campuzano, M. Pedrero, M. I. Pividori, P. Garci, and J. M. Pingarro, "Disposable magnetic DNA sensors for the determination at the attomolar level of a specific enterobacteriaceae family gene," *Anal. Chem.*, vol. 80, no. 21, pp. 8239–8245, 2008.
- [10] R. Saiki, S. Scharf, F. Faloona, K. Mullis, G. Horn, H. Erlich, and N. Arnheim, "Enzymatic amplification of beta-globin genomic sequences and restriction site analysis for diagnosis of sickle cell anemia," *Science*, vol. 230, no. 4732, pp. 1350–1354.
- [11] S. Cheng, C. Fockler, W. M. Barnes, and M. Higuchi, "Effective amplification of long targets from cloned inserts and human genomic DNA," *Proc. Nat. Acad. Sci. (PNAS)*, vol. 91, no. 12, pp. 5695–5699, Jun. 7, 1994.
- [12] H. Penga, C. Soellera, N. Vigara, P. A. Kilmartina, M. B. Cannella, G. A. Bowmakera, R. P. Cooneya, and J. Travas-Sejdic, "Label-free electrochemical DNA sensor based on functionalised conducting copolymer," *Biosens. Bioelectron.*, vol. 20, no. 9, pp. 1821–1828, Mar. 2005.
- [13] Y. Xiao, A. A. Lubin, A. J. Heeger, and K. W. Plaxco, "Label-free electronic detection of thrombin in blood serum by using an aptamer-based sensor," *Biosens. Bioelectron.*, vol. 20, no. 9, pp. 1821–1828, Mar. 2005.
- [14] X. C. Zaho, L. Q. Huang, and S. F. Li, "Microgravimetric DNA sensor based on quartz crystal microbalance: comparison of oligonucleotide immobilization methods and the application in genetic diagnosis," *Biosens. Bioelectron.*, vol. 16, no. 2, pp. 85–95, 2001.
- [15] T. G. Drummond, M. G. Hill, and J. K. Barton, "Electrochemical DNA sensors," *Nature Biotechnol.*, vol. 21, no. 10, pp. 1192–1199, Oct. 2003.
- [16] A. Yang, S. R. Jadhav, R. M. Worden, and A. J. Mason, "Compact low-power impedance-to-digital converter for sensor array microsystems," *IEEE J. Solid-State Circuits*, vol. 44, no. 10, pp. 2844–2855, Oct. 2009.
- [17] A. Hassibi and T. H. Lee, "A programmable 0.18  $\mu\text{m}$  CMOS electrochemical sensor microarray for bimolecular detection," *IEEE Sensors J.*, vol. 6, pp. 1380–1388, 2006.
- [18] A. Manickam, A. Chevalier, M. McDermott, A. D. Ellington, and A. Hassibi, "A CMOS electrochemical impedance spectroscopy biosensor array for label-free biomolecular detection," in *IEEE Int. Solid-State Circuits Conf. (ISSCC) Dig. Tech. Papers*, 2009, pp. 438–439.
- [19] A. Hassibi, H. Vikalo, J. L. Riechmann, and B. Hassibi, "Real-time DNA microarray analysis," *Nucleic Acids Research*, vol. 37, no. 20, pp. 1–12, Aug. 2009.
- [20] B. Jang, P. Cao, A. Chevalier, A. Ellington, and A. Hassibi, "A CMOS fluorescence-based biosensor microarray," in *IEEE Int. Solid-State Circuits Conf. (ISSCC) Dig. Tech. Papers*, 2009, pp. 436–437.
- [21] H. Wang, Y. Chen, A. Hassibi, A. Scherer, and A. Hajimiri, "A frequency-shift CMOS magnetic biosensor array with single-bead sensitivity and no external magnet," in *IEEE Int. Solid-State Circuits Conf. (ISSCC) Dig. Tech. Papers*, 2009, pp. 438–439.
- [22] C. Yang, Y. Huang, B. L. Hassler, R. M. Worden, and A. J. Mason, "Amperometric electrochemical microsystem for a miniaturized protein biosensor array," *IEEE Trans. Biomed. Circuits Syst.*, vol. 3, no. 3, pp. 160–168, 2009.
- [23] L. Li, X. Liu, W. A. Qureshi, and A. J. Mason, "CMOS amperometric instrumentation and packaging for biosensor array applications," *IEEE Trans. Biomed. Circuits Syst.*, vol. 5, no. 5, pp. 439–448, 2011.
- [24] R. Genov, M. Stanacevic, M. Naware, G. Cauwenberghs, and N. Thakor, "16-channel integrated potentiostat for distributed neurochemical sensing," *IEEE Trans. Circuits Syst. I*, vol. 53, no. 11, pp. 2371–2376, Nov. 2006.
- [25] M. Nazari, H. Jafari, L. Leng, A. Guenther, and R. Genov, "CMOS neurotransmitter microarray: 96-channel integrated potentiostat with on-die microsensors," *IEEE Trans. Biomed. Circuits Syst.*, vol. 7, no. 3, pp. 338–348, Jun. 2012.

- [26] M. Roham, M. P. Garris, and P. Mohseni, "A wireless IC for time-share chemical and electrical neural recording," *IEEE J. Solid-State Circuits*, vol. 44, no. 10, pp. 3645–3658, Oct. 2009.
- [27] M. Nazari and R. Genov, "A fully differential CMOS potentiostat," in *Proc. IEEE Int. Symp. Circuits Syst. (ISCAS)*, 2009, vol. 2, pp. 2177–2180.
- [28] D. A. Giusto, W. A. Wlassoff, S. Giesebrecht, J. J. Gooding, and G. C. King, "Enzymatic synthesis of redox-labeled RNA and dual-potential detection at DNA-modified electrodes," *Angewandte Chemie Int. Ed.*, vol. 43, pp. 2809–2812, 2004.
- [29] M. Schena, D. Shalon, R. W. Davis, and P. O. Brown, "Quantitative monitoring of gene expression patterns with a complementary DNA microarray," *Science*, vol. 2, no. 5, pp. 467–470, Oct. 1995.
- [30] A. Hassibi and T. H. Lee, "A programmable electrochemical biosensor array in 0.18  $\mu\text{m}$  standard CMOS," in *IEEE Int. Solid-State Circuits Conf. (ISSCC) Dig. Tech. Papers*, 2005, pp. 168–169.
- [31] M. Augustyniak, C. Paulus, R. Brederlow, N. Persike, G. Hartwich, D. Schmitt-Landsiedel, and R. Thewes, "A 24x16 CMOS-based chronocoulometric DNA microarray," in *IEEE Int. Solid-State Circuits Conf. (ISSCC) Dig. Tech. Papers*, 2006, pp. 168–169.
- [32] M. Schienle, C. Paulus, A. Frey, F. Hofmann, B. Holzapfl, P. S. Bauer, and R. Thewes, "A fully electronic DNA sensor with 128 positions and in-pixel A/D conversion," *IEEE J. Solid-State Circuits*, vol. 39, no. 12, pp. 2438–2445, Dec. 2004.
- [33] F. Heer, M. Keller, G. Yu, J. Janata, M. Josowicz, and A. Hierlemann, "CMOS electro-chemical DNA-detection array with on-chip ADC," in *IEEE Int. Solid-State Circuits Conf. (ISSCC) Dig. Tech. Papers*, 2008, pp. 168–169.
- [34] P. M. Levine, P. Gong, R. Levicky, and K. L. Shepard, "Active CMOS sensor array for electrochemical biomolecular detection," *IEEE J. Solid-State Circuits*, vol. 43, no. 8, pp. 1859–1871, Aug. 2008.
- [35] D. M. Garner, H. Bai, P. Georgiou, T. G. Constantinou, S. Reed, L. M. Shepherd, W. Wong, K. T. Lim, and C. Toumazou, "A multichannel DNA SoC for rapid point-of-care gene detection," *IEEE J. Solid-State Circuits*, vol. 43, no. 8, pp. 1859–1871, Aug. 2010.
- [36] C. W. Huang, Y. J. Huang, P. W. Yen, H. T. Hsueh, C. Y. Lin, M. C. Chen, C. Ho, F. L. Yang, H. H. Tsai, H. H. Liao, Y. Z. Juang, C. K. Wang, C. T. Lin, and S. S. Lu, "A fully integrated hepatitis B virus DNA detection SoC based on monolithic polysilicon nanowire CMOS process," in *IEEE Symp. VLSI Circuits Dig. Tech. Papers*, 2012, pp. 124–125.
- [37] L. Soleymani, Z. Fang, E. H. Sargent, and S. O. Kelley, "Programming nucleic acids detection sensitivity using controlled nanostructuring," *Nature Nanotechnol.*, vol. 4, no. 12, pp. 844–848, 2009.
- [38] H. M. Jafari, L. Soleymani, K. Abdelhalim, E. H. Sargent, S. O. Kelley, and R. Genov, "Nanostructured CMOS wireless ultra-wideband label-free DNA analysis SoC," in *IEEE Symp. VLSI Circuits Dig. Tech. Papers*, 2012, pp. 69–70.
- [39] M. Alubaidy, L. Soleymani, K. Venkatakrisnan, and B. Tan, "Femtosecond laser nanostructuring for femtosensitive DNA detection," *Biosens. Bioelectron.*, vol. 33, no. 1, pp. 83–87, Mar. 2012.
- [40] L. Añorga, A. Rebollo, J. Herrán, S. Arana, E. Bandrés, and J. García-Foncillas, "Development of a DNA microelectrochemical biosensor for CEACAM5 detection," *IEEE Sensor J.*, vol. 10, no. 8, pp. 1368–1374, Aug. 2010.
- [41] Y. S. Choi, K. S. Lee, and D. H. Park, "A genomic detection using an indicator-free DNA on a DNA chip microarray," *Appl. Phys.*, vol. 6, no. 4, pp. 772–776, 2006.
- [42] H. M. Jafari, L. Soleymani, and R. Genov, "16-channel CMOS impedance spectroscopy DNA analyzer with dual-slope multiplying ADC," *IEEE Trans. Biomed. Circuits Syst.*, vol. 6, no. 5, pp. 468–478, 2012.
- [43] H. S. Narula and J. G. Harris, "A time-based VLSI potentiostat for ion current measurement," *IEEE Sensors J.*, vol. 6, no. 2, pp. 239–247, 2006.
- [44] M. Ahmadi and G. Jullien, "Current-mirror-based potentiostats for three-electrode amperometric electrochemical sensors," *IEEE Trans. Circuits Syst. I*, vol. 56, no. 7, pp. 1339–1348, 2009.
- [45] S. Hwang and S. Sonkusale, "CMOS VLSI potentiostat for portable environmental sensing applications," *IEEE Sensors J.*, vol. 10, pp. 820–821, 2010.
- [46] S. Ayers, K. D. Gillis, M. Lindau, and B. A. Minch, "Design of a CMOS potentiostat circuit for electrochemical detector arrays," *IEEE Trans. Circuits Syst. I*, vol. 54, no. 4, pp. 736–744, Apr. 2007.
- [47] A. Zeki and H. Kuntman, "Accurate and high output impedance current mirror suitable for CMOS current output stages," *IEEE Sensors J.*, vol. 6, no. 12, pp. 1380–1388, 2006.
- [48] A. J. Chen, "Multibit delta-sigma modulator with noise-shaping dynamic element matching," *IEEE Trans. Circuits Syst. I*, vol. 56, no. 6, pp. 1125–1133, Jun. 2009.
- [49] P. P. Mercier, D. C. Daly, and A. P. Chandrakasan, "An energy-efficient all-digital UWB transmitter employing dual capacitively-coupled pulse-shaping drivers," *IEEE J. Solid-State Circuits*, vol. 44, no. 6, pp. 1679–1688, Jun. 2009.
- [50] Y. Park and D. Wentzloff, "An all-digital 12 pJ/pulse IR-UWB transmitter synthesized from a standard cell library," *IEEE J. Solid-State Circuits*, vol. 46, no. 5, pp. 1147–1157, May 2011.
- [51] P. P. Mercier, M. Bhardwaj, D. C. Daly, and A. P. Chandrakasan, "A low-voltage energy-sampling IR-UWB digital baseband employing quadratic correlation," *IEEE J. Solid-State Circuits*, vol. 45, no. 6, pp. 1209–1219, Jun. 2010.
- [52] M. J. Milgrew, "A 16x16 CMOS proton camera array for direct extracellular imaging of hydrogen-ion activity," in *IEEE Int. Solid-State Circuits Conf. (ISSCC) Dig. Tech. Papers*, 2008, pp. 590–638.
- [53] H.-S. Wong and M. White, "A self-contained CMOS integrated pH sensor," in *Proc. IEEE Int. Electron Devices Meeting (IEDM)*, 1988, pp. 658–661.
- [54] H. M. Jafari and R. Genov, "Chopper-stabilized bidirectional current acquisition circuits for electrochemical amperometric biosensors," *IEEE Trans. Circuits Syst. I*, vol. 60, no. 5, pp. 1149–1157, May 2013.
- [55] A. J. Bard and L. R. Faulkner, *Electrochemical Methods: Fundamentals and Applications*, 2nd ed. New York, NY, USA: Wiley, 2000.
- [56] B. Razavi, *Design of Analog CMOS Integrated Circuits*. Boston, MA, USA: McGraw-Hill, 2001.
- [57] Integrated DNA Technologies, May 15, 2013 [Online]. Available: <http://www.idtdna.com/>
- [58] Basi RE-5B, May 15, 2013 [Online]. Available: <http://www.basinc.com/>



**Hamed Mazhab Jafari** received the B.Eng. and M.A.Sc. degrees in electrical engineering from McMaster University, Hamilton, ON, Canada, in 2004 and 2006, respectively, and the Ph.D. degree in electrical and computer engineering from the University of Toronto, Toronto, Ontario, Canada, in 2013. His M.A.Sc. thesis focused on low-power ultra-wideband CMOS front-ends and ultra-wideband antennas. He is currently working toward the Ph.D. degree at the University of Toronto, Toronto, Ontario, Canada. His Ph.D. thesis focus is on CMOS

DNA analysis SoC.

He has held internship positions at Kapik Integration, where he worked on low-power mixed-signal circuits. Since 2011, he has been with Snowbush IP, Toronto, ON, Canada, where he focuses on research and development of next-generation high-speed wireline communication systems.



**Karim Abdelhalim** (S'06) received the B.Eng. and M.A.Sc. degrees in electrical engineering from Carleton University, Ottawa, Ontario, Canada, in 2005 and 2007, respectively, and the Ph.D. degree in electrical and computer engineering from the University of Toronto, Toronto, Ontario, Canada, in 2013, where he focused on wireless neural recording and stimulation SoCs and their application in monitoring and treatment of intractable epilepsy.

He is currently a senior staff design scientist at Broadcom Corporation, Irvine, CA, USA, since 2011, where he is involved with the design of mixed-signal ICs for Ethernet applications. From July 2010 to October 2010, he also worked as a mixed-signal design engineering intern at Broadcom Corporation, Irvine.

Dr. Abdelhalim is a recipient of the Alexander Graham Bell Canada Graduate Scholarship awarded by the Natural Sciences and Engineering Research Council of Canada (NSERC) from 2007 to 2010. He also held the Ontario Graduate Scholarship (OGS) in 2005, the NSERC CGS-M in 2008 and the Ontario Graduate Scholarships in Science and Technology (OGSST) in 2011. He worked as a volunteer at the IEEE International Solid-State Circuits Conference (ISSCC) from 2008 to 2011.



**Leyla Soleymani** received the Ph.D. degree in electrical and computer engineering from the University of Toronto, Toronto, ON, Canada, in 2010.

She is currently an Assistant Professor in the Department of Engineering Physics and School of Biomedical Engineering, McMaster University, Hamilton, ON, Canada. Her research interests include development of new hierarchical materials and combining different micro/nanofabrication technologies for building chip-based biosensors.



**Edward H. Sargent** received the B.Sc. degree in engineering physics from Queen's University in 1995 and the Ph.D. degree in electrical and computer engineering from the University of Toronto in 1998.

He is Professor and Canada Research Chair in Nanotechnology at the University of Toronto, where he also serves as Vice Dean for Research for the Faculty of Applied Science and Engineering.

Prof. Sargent is a Fellow of the AAAS "...for distinguished contributions to the development of solar cells and light sensors based on solution-processed semiconductors," and a Fellow of the IEEE "... for contributions to colloidal quantum dot optoelectronic devices." He is a KAUST Investigator; founder and CTO of InVisage Technologies of Menlo Park, CA, USA; and a cofounder of Xagenic Inc.



**Shana O. Kelley** received the B.S. degree from Seton Hall University, South Orange, NJ, USA, in 1994 and the Ph.D. degree in chemistry from the California Institute of Technology, Pasadena, CA, USA, in 1999.

She is a scientist and Professor of biochemistry at the University of Toronto's Faculty of Pharmacy and Faculty of Medicine. She is also the Director of the Biomolecular Sciences Division and the Kelley Laboratory.

Prof. Kelley was named among the Top 100 Innovators by MIT's Technology Review while she was a Professor at Boston College.



**Roman Genov** (S'96–M'02–SM'11) received the B.S. degree in electrical engineering from Rochester Institute of Technology, Rochester, NY, USA, in 1996, and the M.S.E. and Ph.D. degrees in electrical and computer engineering from The Johns Hopkins University, Baltimore, MD, USA, in 1998 and 2002, respectively.

He held engineering positions at Atmel Corporation, Columbia, MD, USA, in 1995 and Xerox Corporation, Rochester, NY, USA, in 1996. He was a visiting researcher at the Laboratory of Intelligent Systems at the Swiss Federal Institute of Technology (EPFL), Lausanne, Switzerland, in 1998 and at the Center for Biological and Computational Learning at the Massachusetts Institute of Technology, Cambridge, MA, USA, in 1999. He is presently an Associate Professor in the Department of Electrical and Computer Engineering at the University of Toronto, Ontario, Canada. His research interests include analog and digital VLSI circuits, systems and algorithms for energy-efficient signal processing with applications to electrical, chemical and photonic sensory information acquisition, biosensor arrays, brain-silicon interfaces, parallel signal processing, adaptive computing for pattern recognition, and implantable and wearable biomedical electronics.

Dr. Genov was a co-recipient of Best Paper Award of IEEE Biomedical Circuits and Systems Conference, Best Student Paper Award of IEEE International Symposium on Circuits and Systems, Best Paper Award of IEEE Circuits and Systems Society Sensory Systems Technical Committee, Brian L. Barge Award for Excellence in Microsystems Integration, MEMSCAP Microsystems Design Award, DALSA Corporation Award for Excellence in Microsystems Innovation, and Canadian Institutes of Health Research Next Generation Award. He was a Technical Program Co-chair at IEEE Biomedical Circuits and Systems Conference. He was an Associate Editor of IEEE TRANSACTIONS ON CIRCUITS AND SYSTEMS II: EXPRESS BRIEFS and *IEEE Signal Processing Letters*. He is currently an Associate Editor of IEEE TRANSACTIONS ON BIOMEDICAL CIRCUITS AND SYSTEMS.